The CIB-lensing bispectrum: impact on primordial non-Gaussianity and detectability for the *Planck* mission

A. Curto[1,2,3] ⋆ M. Tucci[4] M. Kunz[4,5] E. Martínez-González[1]

[1]*Instituto de Física de Cantabria, CSIC-Universidad de Cantabria, Avda. de los Castros s/n, 39005 Santander, Spain*
[2]*Astrophysics Group, Cavendish Laboratory, Madingley Road, Cambridge CB3 0H3, U.K.*
[3]*Kavli Institute for Cosmology Cambridge, Madingley Road, Cambridge, CB3 0HA, U.K.*
[4]*Département de Physique Théorique and Center for Astroparticle Physics, Université de Genève, 24 quai Ansermet, CH–1211 Genève 4, Switzerland*
[5]*African Institute for Mathematical Sciences, 6 Melrose Road, Muizenberg, 7945, South Africa*

30 March 2021

ABSTRACT

We characterize the Cosmic Infrared Background (CIB)–lensing bispectrum which is one of the contributions to the three-point functions of Cosmic Microwave Background (CMB) maps in harmonic space. We show that the CIB–lensing bispectrum has a considerable strength and that it can be detected with high significance in the *Planck* high–frequency maps. We also present forecasts of the contamination on different shapes of the primordial non-Gaussianity $f_{\rm nl}$ parameter produced by the CIB–lensing bispectrum and by the extragalactic point sources bispectrum in the *Planck* high–resolution CMB anisotropy maps. The local, equilateral and orthogonal shapes are considered for 'raw' single–frequency (i.e., without applying any component separation technique) and foreground–reduced *Planck* temperature maps. The CIB–lensing correlation seems to mainly affect orthogonal shapes of the bispectrum – with $\Delta f_{\rm nl}^{\rm (ort)} = -21$ and -88 for the 143 and 217 GHz bands respectively – while point sources mostly impact equilateral shapes, with $\Delta f_{\rm nl}^{\rm (eq)} = 160, 54$ and 60 at 100, 143 and 217 GHz. However, the results indicate that these contaminants do not induce any relevant bias on *Planck* $f_{\rm nl}$ estimates when foreground–reduced maps are considered: using SEVEM for the component separation we obtain $\Delta f_{\rm nl}^{\rm (ort)} = 10.5$ due to the CIB–lensing and $\Delta f_{\rm nl}^{\rm (eq)} = 30.4$ due to point sources, corresponding to 0.3σ and 0.45σ in terms of the *Planck* 2013 $f_{\rm nl}$ uncertainty. The component separation technique is, in fact, able to partially clean the extragalactic source contamination and the bias is reduced for all the shapes. We have further developed single- and multiple-frequency estimators based on the Komatsu, Spergel & Wandelt (2005) formalism that can be implemented to efficiently detect this signal.

Key words: methods: data analysis – cosmic microwave background – extragalactic points sources – radio and far–IR: galaxies

1 INTRODUCTION

Primordial non–Gaussianity (NG) in the cosmic microwave background (CMB) radiation has emerged as one of the key tests for the physics of the early Universe, as different models of e.g. inflation predict slightly different deviations from Gaussian primordial fluctuations (see e.g. Bartolo et al. 2004, 2010; Yadav & Wandelt 2010; Liguori et al. 2010; Martínez-González & Planck Collaboration 2012). The latest constraints by the *Planck*[1] satellite put strong constraints on the amount of primordial NG that is present in the data (Planck 2013 results XXIV 2014). But the precision of the *Planck* data requires great care concerning the subtraction of astrophysical contributions to the observed CMB anisotropies (so–called foregrounds). It is important to check all possible contributions for their expected level of contamination of the primordial NG estimate both on sky maps and on foreground-cleaned maps. At least the non-negligible foreground contributions should then be estimated jointly with the primordial ones, which requires the construction of an estimator also for the foregrounds.

⋆ E-mail:curto@ifca.unican.es,acurto@mrao.cam.ac.uk
[1] *Planck* (http://www.esa.int/Planck) is a project of the European Space Agency –ESA– with instruments provided by two scientific consortia funded by ESA member states with contributions from NASA.

Conventionally the CMB anisotropies $\Delta T(\hat{\mathbf{n}})$, being a real-valued random field on the sky sphere, are expanded in spherical harmonics,

$$\Delta T(\hat{\mathbf{n}}) = \sum_{\ell m} a_{\ell m} Y_{\ell m}(\hat{\mathbf{n}}) \tag{1}$$

and schematically we can write the coefficients $a_{\ell m}$ as a superposition of different contributions,

$$a_{\ell m} = \tilde{a}_{\ell m}^{(\text{CMB})} + a_{\ell m}^{(\text{fg})} + n_{\ell m} . \tag{2}$$

Here the first term on the right hand side $\tilde{a}_{\ell m}$ is the primordial contribution, lensed by the intervening large–scale structure. The second term is the contribution due to foregrounds – in general there are both Galactic and extragalactic contributions, but in this paper we will neglect the former and use the term 'foreground' to denote the extragalactic contribution only. For the extragalactic foreground radiation we expect that radio sources dominate at low frequencies, and dusty star–forming galaxies creating the cosmic infrared background (CIB) at high frequencies. The final contribution is instrumental noise, obviously uncorrelated with the CMB and the foreground contributions, that we assume to be Gaussian.

The main tool to study primordial NG is the angular bispectrum, the three–point function of the $a_{\ell m}$,

$$\langle a_{\ell_1 m_1} a_{\ell_2 m_2} a_{\ell_3 m_3} \rangle = G_{\ell_1 \ell_2 \ell_3}^{m_1 m_2 m_3} b_{\ell_1 \ell_2 \ell_3} , \tag{3}$$

where the Gaunt integral (Komatsu & Spergel 2001)

$$G_{\ell_1 \ell_2 \ell_3}^{m_1 m_2 m_3} = \int d^2\hat{\mathbf{n}} Y_{\ell_1 m_1}(\hat{\mathbf{n}}) Y_{\ell_2 m_2}(\hat{\mathbf{n}}) Y_{\ell_3 m_3}(\hat{\mathbf{n}}) \tag{4}$$

takes care of rotational symmetry, and where the non-trivial contribution to the three-point function is encoded in the reduced bispectrum $b_{\ell_1 \ell_2 \ell_3}$.

The product of three $a_{\ell m}$ as written in Eq. (2) will not only contain a primordial contribution. In addition there are additional elements that involve non-primordial terms, some of them already studied in previous works, such as the 'foreground' contribution given schematically by $\langle a_{\ell m}^{(\text{fg})3} \rangle$ (see e.g. Lacasa et al. 2014; Pénin et al. 2013), a contribution from the correlation between the lensing of the CMB and the integrated Sachs–Wolfe (ISW) effect contained in the $\langle \tilde{a}_{\ell m}^{(\text{CMB})3} \rangle$ term (see e.g. Mangilli et al. 2013) and finally a contribution from the correlation between the lensing of the CMB and extragalactic foregrounds. This article is focusing on the last correlation, already detected with a significance of 42σ by Planck 2013 results XVIII (2014) considering statistical errors only (19σ when systematics are included). The CIB–lensing correlation arises as the large–scale structure (LSS) both lenses the CMB and emits the 'foreground' (radio or CIB) radiation. The main contribution here is expected due to the CIB–lensing correlation, as in radio galaxies the clustering signal is highly diluted by the broadness of their luminosity function and of their redshift distribution (e.g., Toffolatti et al. 2005).

In this paper we focus on the CIB–lensing bispectrum, for two reasons. Firstly, in order to ensure that the CMB constraints on primordial NG are accurate, we need to check that the additional contributions are under control. In Planck 2013 results XXIV (2014) the ISW–lensing contribution was fit simultaneously with the primordial contribution, and was shown to be small. Lacasa et al. (2012) and Curto et al. (2013) studied the bispectrum of unresolved point sources and concluded that it is small enough to neglect. However, the situation of the CIB–lensing contribution was so far not investigated in detail, and this paper aims to close this gap. Secondly, probing the non–Gaussianity due to the large–scale structure is not only important for assessing the contamination of the primordial NG, but is also interesting in its own right. The LSS contains important information on the late–time evolution and content of the universe, as well as on the formation and evolution of galaxies. Studying the CIB–lensing correlation is thus not only important to assess the reliability of the constraints on primordial f_{nl}, but also potentially useful for cosmology and astrophysics.

The outline of the paper is as follows: in Section 2 we discuss the CIB–lensing contribution as well as the CIB model that we will use. In Section 3 we estimate the bias on f_{nl} for local, equilateral and orthogonal configurations. We perform the calculation both for raw frequency maps and for linear combinations of maps that remove most of the astrophysical foregrounds, following the SEVEM component separation method used by the *Planck* collaboration (see, e.g. Planck 2013 results XII 2014). We then construct in Sections 4 and 5 an optimal estimator for measuring the CIB–lensing bispectrum and assess the level at which we expect to be able to detect it with *Planck* data before presenting our conclusions in Section 6. In the four attached appendices we provide more details on our model of CIB anisotropies power spectra (including a new parameter fit of the *Planck* measurement of CIB power spectra) and on the calculation of power spectra and bispectra.

2   MODELLING THE CIB AND CIB–LENSING POWER SPECTRA

The interplay between the CMB gravitational lensing and CIB intensity fluctuations are studied in this work in terms of the cross-bispectrum (the so called CIB–lensing bispectrum), its detectability levels and the bias on the primordial non-Gaussianity through the f_{nl} parameter. The observed temperature fluctuations, neglecting other foreground sources, can be expanded at first order as (see e.g. Goldberg & Spergel 1999; Hu 2000):

$$\Delta T(\hat{\mathbf{n}}) = \Delta T_{\text{CMB}}(\hat{\mathbf{n}} + \nabla\phi(\hat{\mathbf{n}})) + \Delta T_{\text{CIB}}(\hat{\mathbf{n}}) \simeq \Delta T_{\text{CMB}}(\hat{\mathbf{n}}) + \nabla(\Delta T_{\text{CMB}}(\hat{\mathbf{n}}))\nabla\phi(\hat{\mathbf{n}}) + \Delta T_{\text{CIB}}(\hat{\mathbf{n}}) , \tag{5}$$

where $\phi(\hat{\mathbf{n}})$ is the lensing potential, $\Delta T_{\text{CMB}}(\hat{\mathbf{n}})$ are the primordial CMB anisotropies and $\Delta T_{\text{CIB}}(\hat{\mathbf{n}})$ are the anisotropies due to the CIB. Going into the spherical harmonic space, the observed anisotropies are:

$$a_{\ell m} = \tilde{a}_{\ell m}^{(\text{CMB})} + a_{\ell m}^{(\text{CIB})} = a_{\ell m}^{(\text{CMB})} + \sum_{\ell' m' \ell'' m''} (-1)^m G_{\ell\ell'\ell''}^{mm'm''} \left[\frac{\ell'(\ell'+1) - \ell(\ell+1) + \ell''(\ell''+1)}{2} a_{\ell' m'}^{(\text{CMB})} \phi_{\ell'' m''} \right] + a_{\ell m}^{(\text{CIB})}, \tag{6}$$
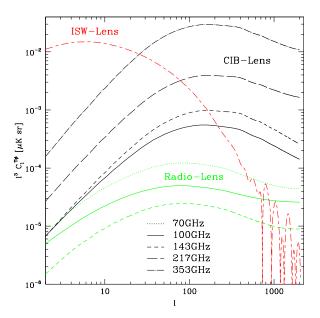
Figure 1. Predicted power spectra of the lensing correlation with ISW (red curve), CIB (black curves) and radio sources (green curves) at the *Planck* frequencies relevant for cosmological analysis.

where $\tilde{a}_{\ell m}^{(\text{CMB})}$, $a_{\ell m}^{(\text{CMB})}$, $a_{\ell m}^{(\text{CIB})}$ and $\phi_{\ell m}$ are the spherical harmonic coefficients of the observed/primordial CMB, CIB and gravitational potential anisotropies, respectively, and $G_{\ell \ell' \ell''}^{m m' m''}$ is the Gaunt coefficient (see Eq. 4).

The angular power spectra of CIB fluctuations and of their cross–correlation with the CMB lensing are typically written in the Limber approximation as (e.g., Song et al. 2003, see also Appendix A for a full derivation):

$$C_\ell^{(\text{CIB})}(\nu, \nu') = \langle a_{\ell m}^{(\text{CIB})*} a_{\ell m}^{(\text{CIB})} \rangle = \int_0^{\chi_*} \frac{d\chi}{\chi^2} W_\nu^{(\text{CIB})}(\chi) W_{\nu'}^{(\text{CIB})}(\chi) \, P_{\text{gg}}(k = \ell/\chi, \chi) \,;$$

$$C_\ell^{(\text{CIB}-\text{Lens})}(\nu) = \langle \phi_{\ell m}^* a_{\ell m}^{(\text{CIB})} \rangle = \int_0^{\chi_*} \frac{d\chi}{\chi^2} W_\nu^{(\text{CIB})}(\chi) W^{(\text{Lens})}(k, \chi) \, P_{\delta \text{g}}(k = \ell/\chi, \chi) \,. \tag{7}$$

The integral is over the comoving distance χ along the line of sight, and extends up to the comoving distance of the last scattering surface $\chi = \chi_*$ (in practice the integral is computed up to redshift 7 because of the negligible contribution of CIB fluctuations at higher redshifts). The $W^{(\text{CIB})}(\chi)$ and $W^{(\text{Lens})}(k, \chi)$ functions are the redshift weights for CIB fluctuations and for the lensing potential ϕ, respectively,

$$W_\nu^{(\text{CIB})}(\chi) = a(\chi) \, \bar{j}_\nu(\chi) \qquad W^{(\text{Lens})}(k, \chi) = 3 \frac{\Omega_m}{a(\chi)} \left(\frac{H_0}{ck} \right)^2 \frac{\chi_* - \chi}{\chi_* \chi} \,, \tag{8}$$

where $a(\chi)$ is the scale factor and $\bar{j}_\nu(\chi)$ is the mean CIB emissivity at frequency ν as a function of χ:
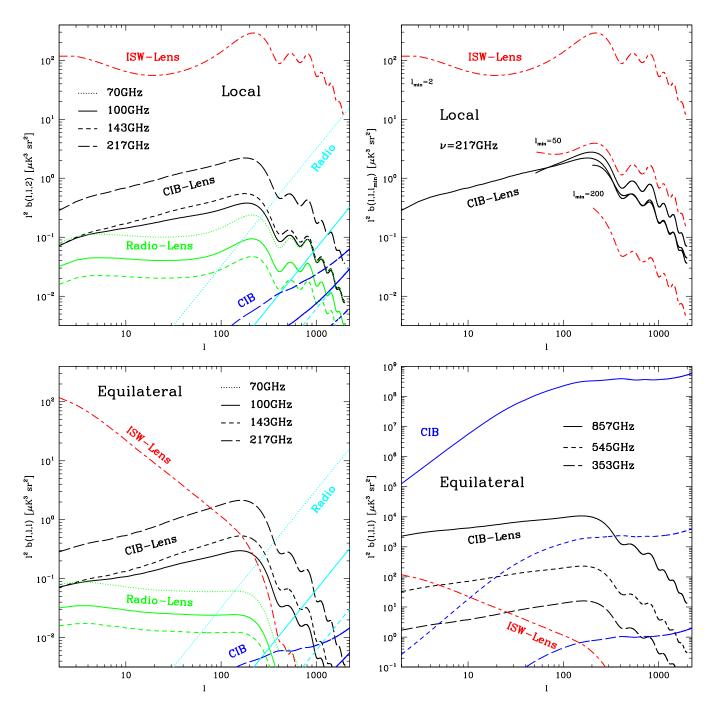
$$\bar{j}_\nu(\chi) = (1 + z) \left(\frac{d\chi}{dz} \right)^{-1} \int_0^{S_c} S \frac{d^2 N}{dS dz} dS \,. \tag{9}$$

Here $d^2 N / dS dz$ denotes galaxies number counts per interval of flux density and redshift, and S_c is the flux limit above which sources are subtracted or masked[2]. We compute the redshift evolution of the CIB emissivity from the model of galaxy evolution of Béthermin et al. (2011)[3]. This is a backward evolution model based on parametric luminosity functions for two populations of galaxies: normal and starburst galaxies. It uses spectral energy distribution templates for the two galaxy populations taken from the Lagache et al. (2004) library. The model is described by 13 free parameters and the best–fit values are computed using observational number counts and luminosity functions from mid–infrared to millimetre wavelengths (Béthermin et al. 2011). This CIB model was previously used by Pénin et al. (2012) before and then applied to *Planck* results (Planck early results XVIII 2011; Planck 2013 results XXX 2014) in order to compute CIB and CIB–lensing power spectra.

In Eq. (7), $P_{\text{gg}}(k, \chi)$ and $P_{\delta \text{g}}(k, \chi)$ are respectively the 3D power spectrum of galaxies and of the cross–correlation between galaxies and the dark matter (DM) density field. In the context of the halo model (Scherrer & Bertschinger 1991; Seljak 2000; Scoccimarro et al. 2001; Cooray & Sheth 2002), the power spectra are the sum of the contribution of the clustering in one single halo (1–halo term) and in two

---

[2] Hereafter, we use as flux limit for the *Planck* mission the 90% completeness level of the *Planck* Catalogue of Compact Sources, given in Planck 2013 results XXVIII (2014).

[3] We use number counts of the so–called *mean model*, see the http://www.ias.u-psud.fr/irgalaxies/ web page.

Figure 2. Predicted bispectra for the local (*upper panels*) and equilateral ($\ell_1 = \ell_2 = \ell_3$; *lower panels*) configurations. Contributions are as in Figure 1, plus bispectra from radio sources (cyan curves) and IR galaxies (blue curves). Frequencies are indicated inside the plots. In the *upper left panel*, "local" bispectra are plotted at different frequencies (from 70 to 217 GHz) and for $\ell_1 = \ell_2$ and $\ell_3 = \ell_{\min} = 2$; in the *upper right panel*, they are plotted at 217 GHz for $\ell_3 = \ell_{\min} = 2,\ 50,\ 200$.

different halos (2–halo term):

$$P_{\mathrm{gg}}(k) = P^{1h}_{\mathrm{gg}}(k) + P^{2h}_{\mathrm{gg}}(k) \qquad P_{\delta \mathrm{g}}(k) = P^{1h}_{\delta \mathrm{g}}(k) + P^{2h}_{\delta \mathrm{g}}(k)$$

$$P^{1h}_{\mathrm{gg}}(k) = \int dM\, n(M) \frac{\langle N_{\mathrm{gal}}(N_{\mathrm{gal}} - 1)\rangle}{\bar{n}^2_{\mathrm{gal}}} u^2(k, M) \qquad P^{1h}_{\delta \mathrm{g}}(k) = \int dM\, n(M) \frac{M}{\bar{\rho}} \frac{\langle N_{\mathrm{gal}}\rangle}{\bar{n}_{\mathrm{gal}}} u^2(k, M)$$

$$P^{2h}_{\mathrm{gg}}(k) = P_{\mathrm{lin}}(k) \left[\int dM\, n(M) b(M) \frac{\langle N_{\mathrm{gal}}\rangle}{\bar{n}_{\mathrm{gal}}} u(k, M) \right]^2 \qquad P^{2h}_{\delta \mathrm{g}}(k) = P_{\mathrm{lin}}(k) \int dM_1\, n(M_1) b(M_1) \frac{M_1}{\bar{\rho}} u(k, M) \times$$

$$\times \int dM_2\, n(M_2) b(M_2) \frac{\langle N_{\mathrm{gal}}\rangle}{\bar{n}_{\mathrm{gal}}} u(k, M_2) \qquad (10)$$

The main inputs required for the calculations of $P_{\rm gg}(k)$ and $P_{\delta \rm g}(k)$ are: (i) the mass function $n(M)$ of DM halos –we use the mass function fit of Tinker et al. (2008) with its associated prescription for the halo bias, $b(M)$ (see Tinker et al. 2010)–; (ii) the distribution of DM within halos, $u(k,M)$, –we use the NFW (Navarro et al. 1997) profile–; and (iii) the Halo Occupation Distribution (HOD), that is a statistical description of how DM halos are populated with galaxies. We model the HOD using a central-satellite formalism (e.g., Kravtsov et al. 2004; Zheng et al. 2005): it introduces a distinction between central galaxies, which lies at the centre of the halo, and satellite galaxies that populate the rest of the halo and are distributed in proportion to the halo mass profile. The mean number of galaxies in a halo of mass M is thus written as $\langle N_{\rm gal} \rangle = \langle N_{\rm cen} \rangle + \langle N_{\rm sat} \rangle$. Following Tinker & Wetzel (2010), the mean occupation functions of central and satellite galaxies are:

$$\langle N_{\rm cen} \rangle = \frac{1}{2} \left[1 + {\rm erf} \left(\frac{\log M - \log M_{\rm min}}{\sigma_{\log M}} \right) \right], \tag{11}$$

and

$$\langle N_{\rm sat} \rangle = \frac{1}{2} \left[1 + {\rm erf} \left(\frac{\log M - \log 2 M_{\rm min}}{\sigma_{\log M}} \right) \right] \left(\frac{M}{M_{\rm sat}} \right)^{\alpha_{\rm sat}}, \tag{12}$$

where $M_{\rm min}$, $\alpha_{\rm sat}$, $M_{\rm sat}$ and $\sigma_{\log M}$ are free parameters. Within this parametrisation, most of the halos with $M \gtrsim M_{\rm min}$ contain a central galaxy. For satellite galaxies the mass threshold is chosen to be twice $M_{\rm min}$, so that halos with a low probability of having a central galaxy are unlikely to contain a satellite galaxy. The number of satellite galaxies grows with a slope $\alpha_{\rm sat}$ for high–mass halos. Moreover, assuming a Poisson distribution for $N_{\rm sat}$, we can write $\langle N_{\rm gal}(N_{\rm gal} - 1) \rangle = 2\langle N_{\rm sat} \rangle + \langle N_{\rm sat} \rangle^2$ (Zheng et al. 2005). Finally, in Eq. (10), $\bar{\rho}$ is the background density, $\bar{n}_{\rm gal}$ is the mean number of galaxies given by $\int dM n(M) \langle N_{\rm gal} \rangle$, and $P_{\rm lin}$ is the linear DM power spectrum.

Following the analysis in Planck early results XVIII (2011), we restrict the free HOD parameters to only $M_{\rm min}$ and $\alpha_{\rm sat}$ by imposing $M_{\rm sat} = 3.3 M_{\rm min}$ and $\sigma_{\log M} = 0.65$. Moreover, because of the uncertainty of the evolution model of galaxies at high redshift, the effective mean emissivity $j_{\rm eff}$ at $z > 3.5$ is also constrained from data as an extra free parameter (see Appendix B, and Planck early results XVIII 2011). We find the best–fit values of the model parameters (i.e., $M_{\rm min}$, $\alpha_{\rm sat}$ and $j_{\rm eff}$) using the recent *Planck* measurements of the CIB power spectra (Planck 2013 results XXX 2014): the results are in good agreement with values of Planck early results XVIII (2011). Details and results of the analysis are provided in Appendix B. As shown in Figures B1–B2 of Appendix B, the model is able to reproduce in a quite remarkable way *Planck* measurements both for the auto– and cross– CIB spectra and for the CIB–lensing spectra.

2.1 Computing CIB and CIB–lensing spectra at very large scales

At the very large scales, i.e. at $\ell \lesssim 10$, the Limber approximation used in Eq. (7) is not further valid. Here we provide the general expression for CIB and CIB–lensing power spectra, that we use for the angular scales ranging from $\ell = 2$ to 40:

$$
\begin{aligned}
C_\ell^{\rm (CIB)}(\nu, \nu') &= \frac{2}{\pi} \int dk \, k^2 \int_0^{\chi_*} d\chi \, W_\nu^{\rm (CIB)}(\chi) j_\ell(k\chi) P_{\rm gg}^{1/2}(k, \chi) \int_0^{\chi_*} d\chi' \, W_{\nu'}^{\rm (CIB)}(\chi') j_\ell(k\chi') P_{\rm gg}^{1/2}(k, \chi') \\
C_\ell^{\rm (CIB-Lens)}(\nu) &= \frac{2}{\pi} \int dk \, k^2 \int_0^{\chi_*} d\chi \, W_\nu^{\rm (CIB)}(\chi) j_\ell(k\chi) P_{\rm gg}^{1/2}(k, \chi) \int_0^{\chi_*} d\chi' \, W^{\rm (Lens)}(k, \chi') j_\ell(k\chi') P_{\delta\delta}^{1/2}(k, \chi'),
\end{aligned}
\tag{13}
$$

where $j_\ell(x)$ are the spherical Bessel functions and $P_{\delta\delta}(k, \chi)$ is the power spectrum of the DM density field respectively. The expression for the CIB–lensing correlation power spectrum has been derived in Appendix A, following the procedure developed in Lewis & Challinor (2006) for the ISW–Lensing power spectrum (the CIB spectrum can be derived in a similar way). We have verified that in the Limber approximation power spectra are typically overestimated by a factor 1.5 at $\ell = 2$.

2.2 Correlation of radio sources with the CMB lensing

Intensity fluctuations produced by extragalactic radio sources at cm/mm wavelengths are dominated by the shot–noise term due to bright objects. The contribution from the radio sources clustering is expected to be significant for faint objects, i.e. for flux densities $S \lesssim 10$ mJy (González-Nuevo et al. 2005; Toffolatti et al. 2005). This is actually observed in low–frequency surveys like the NVSS survey (Condon et al. 1998), which have been found to be fair tracers of the underlying density field at redshifts $z \lesssim 2$ (see, e.g., Boughn & Crittenden 2005; Vielva et al. 2006; Planck 2013 results XIX 2014). Therefore, although small, we expect some level of correlation between the signal from radio sources and the CMB lensing potential, which is primarily induced by dark matter halos at $1 \lesssim z \lesssim 3$.

In order to estimate this contribution we use the same formalism as for the CIB. The radio–lensing power spectrum is given therefore by

$$C_\ell^{\rm (Radio-Lens)}(\nu) = \int_0^{\chi_*} \frac{d\chi}{\chi^2} W_\nu^{\rm (Radio)}(\chi) W^{\rm (Lens)}(k, \chi) P_{\delta \rm g}(k = \ell/\chi, \chi) \quad \text{with} \quad W_\nu^{\rm (Radio)}(\chi) = a(\chi) \bar{j}_\nu(\chi). \tag{14}$$

The mean emissivity of radio sources is computed from Eq. (9) with number counts $d^2N/dSdz$ provided by the model described in Tucci et al. (2011). We estimate the integral starting from $S = 10^{-5}$ Jy, which nearly corresponds to the limit of validity of the model. At lower flux densities, we expect number counts to have a break at $\sim \mu$Jy, and that the contribution from fainter sources, although maybe not completely negligible, should not affect the conclusions of our analysis.

The power spectrum $P_{\delta \rm g}(k, \chi)$ is computed as the sum of the 1–halo and 2–halo terms, see Eq. (10). Unlike the CIB, we assume that the mean number of galaxies per halo, $\langle N_{\rm gal} \rangle$, is equal to 1 if the halo mass is larger than some threshold $M_{\rm min}$, and otherwise is zero. This choice is motivated by the fact that we are taking into account only the most powerful radio objects that are typically associated to

the centre of dark matter halos. This assumption also agrees with results from Marcos-Caballero et al. (2013) for the NVSS survey: they found that the average number of galaxies within a halo of mass M can be described by a step function with the mass threshold in the range $12.3 \lesssim \log(M_{\min}/M_{\odot}) < 12.4$. We take $\log(M_{\min}/M_{\odot}) = 12.34$. We have also verified that our results are only weakly dependent on the value of $M_{\min}$. The radio-lensing power spectra for this parametrization are shown in Fig. 1. Chatterjee et al. (2012) studied the HOD of AGNs using cosmological hydrodynamic simulations: they found that the mean occupation function can be modelled as a softened step function for central AGNs (same as our Eq. 11) and as a power law for satellite AGNs. Using their occupation functions for redshift $z = 1$ and for the brightest sources ($L_{\rm bol} \geqslant 10^{42}$ erg s^{-1}; see their Table 2), we find radio–lensing power spectra in very good agreement with the ones shown in Fig. 1. On the other hand, their occupation functions for fainter AGNs give significantly lower power spectra.

We want to stress however that our estimates for the radio–lensing power spectra should be taken only as indicative of the level of the signal, due to the large uncertainties in modelling radio sources. It is outside of the aim of this work to provide more accurate predictions for this component.

2.3   Forecasts for non–primordial bispectra

Due to the strong clustering of Infrared (IR) galaxies, CIB fluctuations produce a non–constant bispectrum that we compute with the following prescription (see e.g. Argüeso et al. 2003; Lacasa et al. 2012; Curto et al. 2013):

$$b^{(\rm CIB)}_{\ell_1\ell_2\ell_3} = b^{(\rm CIB)}_{\rm sn} \sqrt{\frac{C^{(\rm CIB)}_{\ell_1} C^{(\rm CIB)}_{\ell_2} C^{(\rm CIB)}_{\ell_3}}{(C^{(\rm CIB)}_{\rm sn})^3}} , \tag{15}$$

where $C^{(\rm CIB)}_{\rm sn}$ and $b^{(\rm CIB)}_{\rm sn}$ are the shot–noise contributions to CIB power spectra and bispectra (see Appendix C).

Additionally the coupling of the weak lensing of the CMB with CIB anisotropies leads also to a bispectrum that is, in the reduced form, given by (Goldberg & Spergel 1999; Cooray & Hu 2000; Lewis et al. 2011)

$$b^{(\rm CIB-Lens)}_{\ell_1\ell_2\ell_3} = \frac{\ell_1(\ell_1+1) - \ell_2(\ell_2+1) + \ell_3(\ell_3+1)}{2} \tilde{C}^{(\rm CMB)}_{\ell_1} C^{(\rm CIB-Lens)}_{\ell_3} + (5 \text{ perm}) , \tag{16}$$

where $\tilde{C}^{(\rm CMB)}_{\ell}$ is the lensed CMB power spectrum[4]. Eq. (16) was derived for the first time by Goldberg & Spergel (1999) for a generic tracer of the matter distribution expanding lensed CMB temperature fluctuations $\Delta T(\hat{\bf n}) = \Delta T(\hat{\bf n} + \nabla\phi(\hat{\bf n}))$ to the first order in ϕ. In the original form they used the unlensed $C^{(\rm CMB)}_{\ell}$ in the right-hand part of the equation. Lewis et al. (2011) showed instead that, when higher–order terms are taken into account, the correct equation requires to use the lensed CMB power spectrum.

Bispectra induced by the correlation of the CMB lensing potential with a tracer of the matter distribution differ only for the shape of the cross–power spectrum of the lensing and the matter tracer. In Fig. 1 we compare the cross–power spectra for the case of ISW and extragalactic sources. We see that the ISW–lensing power spectrum is the most relevant one on scales larger than few degrees (it is 2–3 order of magnitude larger than other spectra at $\ell = 2$), but rapidly decreases at $\ell \gtrsim 100$. On these scales the CIB–lensing power spectrum dominates even at frequencies as low as 100–143 GHz. On the contrary, as expected, the radio–lensing correlation produces just a sub-dominant contribution at all the angular scales and therefore it will not be taken into account in the following analysis.

The ISW–lensing correlation is found to be a significant contaminant for *Planck* mainly on local primordial NG: Planck 2013 results XXIV (2014) estimated a bias on $f_{\rm nl}$ of 7.1, 0.4 and -22 (1.22, 0.01, -0.56 in σ units) for the local, equilateral and orthogonal shape, respectively. In Fig. 2 we compare the non–primordial bispectra for the local and the equilateral configurations at frequencies between 70 and 217 GHz (the orthogonal and equilateral configurations are very similar). We can see that for the local shape the ISW–lensing bispectrum is about two orders of magnitude larger than the CIB–lensing contribution for $\ell_{\min} = 2$. However, whereas the latter changes very moderately with $\ell_{\min}$, the ISW–lensing bispectrum is strongly reduced increasing $\ell_{\min}$, e.g., by a factor $\sim 10^2$ and 10^3 for $\ell_{\min} = 50$ and 200 respectively. For the other shapes, the ISW–lensing bispectrum decreases rapidly with the angular scale ℓ, and the dominant contributions come from the CIB–lensing correlation at $\ell \gtrsim 100$ and from extragalactic sources at very small scales ($\ell \gtrsim 1000$). Fig. 2 shows that the CIB and its correlation with the CMB lensing could be a non-negligible contaminant in NG studies, and motivates the following deeper analysis.

Finally, in Fig. 2 we also consider the different contributions for the equilateral shape at the highest *Planck* frequencies. This is interesting in terms of a possible detection of the CIB-lensing bispectrum. Due to its strong signal at these frequencies, it should be detectable with high significance for *Planck* at $\nu \geqslant 217$ GHz. However, IR galaxies give rise themselves to a strong contribution at high frequencies and they can be therefore a strong contaminant for the detection of the CIB–lensing bispectrum. We discuss later how to tackle this problem.

3   THE CIB-LENSING BISPECTRUM BIAS ON THE PRIMORDIAL NON-GAUSSIANITY

To continue with our study of the bispectra presented above, we consider three scenarios for the estimation of the $f_{\rm nl}$ bias due to the CIB-lensing correlation: (i) raw per-frequency maps, which in particular contain CMB lensed signal plus CIB and radio point source contributions plus instrumental noise, (ii) foreground-reduced (clean) maps per frequency and (iii) a combination of clean maps. Galactic foregrounds are not taken into account. We use *Planck* "ideal" instrumental characteristics – i.e. isotropic noise, spherically symmetric beams, full sky

---

[4] We have computed the lensed and unlensed power spectra and the CMB-lensing cross-spectrum using the cosmological parameters that best fit the combined WMAP and *Planck* 2013 data (referred as 'Planck+WP+highL' in Planck 2013 results XVI 2014) using the latest version of CAMB (Lewis et al. 2000).
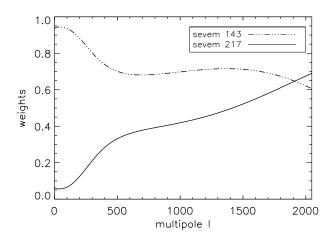
Figure 3. The SEVEM component separation weights $w_\ell^{(\nu_i)}$ for the combination of 143 and 217 GHz maps. Please notice that the weights include the deconvolution/convolution process to reach the final 5 arcmin resolution.

coverage – that are summarized in Table 1. As a representative component separation technique already used by the *Planck* collaboration, and for reason of simplicity, we select SEVEM (Leach et al. 2008; Fernández-Cobos et al. 2012; Planck 2013 results XII 2014). This cleaning technique is based on a template fitting approach. The templates used by SEVEM are constructed using only *Planck* data and there are no assumptions on the foregrounds or noise levels. The templates are constructed by taking the difference of two close *Planck* frequency maps previously smoothed to a common resolution[5]. This template is therefore clean of CMB signal. The SEVEM foreground-reduced map at a given frequency is computed by subtracting from the raw map at that frequency a linear combination of selected templates. The linear coefficients are computed by minimising the variance of the final map. SEVEM is linear and therefore the $a_{\ell m}$ coefficients of a cleaned map can be written as a linear combination of the coefficients of the raw maps involved in the cleaning process. The SEVEM cleaned maps used in this paper are the 143 and 217 GHz maps, also considered in the non-Gaussianity analyses performed in Planck 2013 results XXIII (2014); Planck 2013 results XXIV (2014). These two maps are computed with 4 templates – two corresponding to the LFI channels, namely the 30-44 and 44-70 templates, and two corresponding to the HFI channels, namely the 545-353 and the 857-545 templates. These templates take into account different Galactic and extra-Galactic foregrounds at low and high frequencies and their residual amplitude present in the data is minimised.

The spherical harmonic coefficients of maps for the three cases mentioned above are given by:

- (i) *Planck* raw maps per frequency

$$a_{\ell m}^{(\text{raw},\nu)} = \left[\tilde{a}_{\ell m}^{(\text{prim})} + a_{\ell m}^{(\text{CIB},\nu)} + a_{\ell m}^{(\text{Radio},\nu)}\right]b_\ell^{(\nu)} + a_{\ell m}^{(\text{noise})}, \tag{17}$$

- (ii) *Planck* clean maps per frequency

$$a_{\ell m}^{(\text{clean},\nu)} = \sum_{i=1}^{9} f_{\nu_i}^{(\nu)} a_{\ell m}^{(\text{raw},\nu_i)}, \tag{18}$$

- (iii) *Planck* combined clean map

$$a_{\ell m}^{(\text{comb})} = \sum_{i=5}^{6} w_\ell^{(\nu_i)} a_{\ell m}^{(\text{clean},\nu_i)}. \tag{19}$$

where $b_\ell^{(\nu)}$ is the beam for each frequency channel ν, $f_{\nu_i}^{(\nu)}$ are the SEVEM component separation weights per frequency ν, and $w_\ell^{(\nu_i)}$ are the SEVEM component separation weights for the combined map. We use the raw maps in the frequency range between 100 and 353 GHz. Frequencies lower than 100 GHz have a negligible IR contribution. At frequencies higher than 353 GHz, the CIB signal is clearly dominant over the CMB and the corresponding cosmic variance completely masks the CIB–lensing signal. The low and high frequency maps are nonetheless useful as templates to clean the central frequency maps in Eq. (18) where the sum runs over all nine *Planck* frequencies from frequency 1 = 30 GHz to frequency 9 = 857 GHz. These maps are only produced for 143 GHz (frequency 5) and 217 GHz (frequency 6). The weights for the SEVEM templates needed to construct the foreground-reduced maps are given in Table 2 and are based on Planck 2013 results XII (2014). Finally the SEVEM combined map is computed using the weights given in Fig. 3 following Eq. (19), reaching a resolution of 5 arcmin.

---

[5] E.g. the 44-70 template would be constructed by subtracting the 44 and 70 GHz maps previously smoothed to a common beam defined as the product of the beams of the two maps in spherical harmonics space, $b_\ell^{\nu=44}$ and $b_\ell^{\nu=70}$.

Table 1. *Planck* instrumental characteristics based on published information (see Tables 2 and 6 in Planck 2013 results I 2014).

Channel index	1	2	3	4	5	6	7	8	9
Frequency (GHz)	30	44	70	100	143	217	353	545	857
Beam FWHM (arcmin)	33	28	13	10	7	5	5	5	5
σ_{noise} per pixel (μK)	9.2	12.5	23.2	11.0	6.0	12.0	43.0	897.5	37178.6
N_{side}	1024	1024	1024	2048	2048	2048	2048	2048	2048

Table 2. Linear coefficients and templates used to clean individual frequency maps with SEVEM (see Table C1 in Planck 2013 results XII 2014).

Template	30-44	44-70	545-353	857-545
$f_{\nu_i}^{(143)}$	-2.14×10^{-2}	-1.23×10^{-1}	-7.52×10^{-3}	6.67×10^{-5}

Template	30-44	44-70	545-353	857-545
$f_{\nu_i}^{(217)}$	1.03×10^{-1}	-1.76×10^{-1}	-1.84×10^{-2}	1.21×10^{-4}

3.1 Power spectrum

The power spectrum for the three considered cases is:

- (i) *Planck* raw maps per frequency

$$C_\ell^{(\nu)} = \left[b_\ell^{(\nu)}\right]^2 \left[\tilde{C}_\ell^{(\text{CMB})} + C_\ell^{(\text{CIB},\nu)} + C_\ell^{(\text{Radio},\nu)}\right] + C_\ell^{(\text{noise},\nu)}, \tag{20}$$

- (ii) *Planck* cleaned maps per frequency

$$C_\ell^{(\text{clean},\nu)} = \sum_{\{i,j\}=1}^{9} f_{\nu_i}^{(\nu)} f_{\nu_j}^{(\nu)} b_\ell^{(\nu_i)} b_\ell^{(\nu_j)} \left[\tilde{C}_\ell^{(\text{CMB})} + C_\ell^{(\text{CIB},\nu_i,\nu_j)} + C_\ell^{(\text{Radio},\nu_i,\nu_j)}\right] + \sum_{i=1}^{9} \left[f_{\nu_i}^{(\nu)}\right]^2 C_\ell^{(\text{noise},\nu_i)}, \tag{21}$$

- (iii) *Planck* combined cleaned maps

$$C_\ell^{(\text{comb})} = \sum_{\{i,j\}=1}^{9} g_\ell^{(\nu_i)} g_\ell^{(\nu_j)} b_\ell^{(\nu_i)} b_\ell^{(\nu_j)} \left[\tilde{C}_\ell^{(\text{CMB})} + C_\ell^{(\text{CIB},\nu_i,\nu_j)} + C_\ell^{(\text{Radio},\nu_i,\nu_j)}\right] + \sum_{i=1}^{9} \left[g_\ell^{(\nu_i)}\right]^2 C_\ell^{(\text{noise},\nu_i)}, \tag{22}$$

where

$$g_\ell^{(\nu)} \equiv \sum_{i=5}^{6} w_\ell^{(\nu_i)} f_\nu^{(\nu_i)}, \tag{23}$$

and $C_\ell^{(\text{noise},\nu)}$ is the *Planck* instrumental noise power spectrum at frequency ν.

3.2 Bispectrum

We derive the CIB–lensing, CMB and point sources bispectra for the three considered types of maps.

Table 3. The expected bias Δf_{nl} produced by the CIB-lensing bispectrum for $\ell_{\max} = 2000$ for the raw *Planck* frequency maps between 100 and 353 GHz, the cleaned maps at 143 and 217 GHz and the combination of the two previous cleaned maps. The expected uncertainties on f_{nl} are also reported.

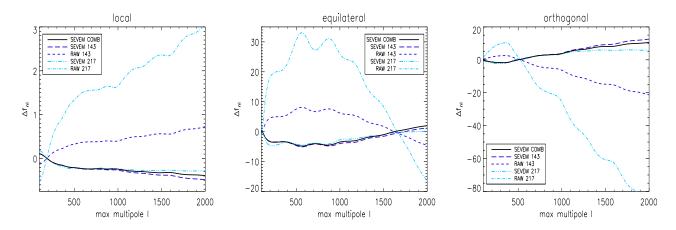| Frequency (GHz)	100	143	217	353	SEVEM 143	SEVEM 217	SEVEM combined
Local Δf_{nl}	0.34	0.73	3.06	13.89	-0.48	-0.28	-0.39
Local $\sigma(f_{\text{nl}})$	6.65	5.25	5.55	14.06	5.73	5.87	5.70
Local $\Delta f_{\text{nl}}/\sigma(f_{\text{nl}})$	0.05	0.14	0.55	0.99	-0.08	-0.05	-0.07
Equilateral Δf_{nl}	0.37	-4.56	-16.47	150.23	1.17	0.09	1.99
Equilateral $\sigma(f_{\text{nl}})$	76.39	68.28	71.00	134.60	71.08	72.22	70.97
Equilateral $\Delta f_{\text{nl}}/\sigma(f_{\text{nl}})$	0.00	-0.07	-0.23	1.12	0.02	0.00	0.03
Orthogonal $\Delta(f_{\text{nl}})$	-8.45	-21.31	-87.92	-233.57	12.55	5.78	10.54
Orthogonal $\sigma(f_{\text{nl}})$	39.29	33.19	34.73	76.33	35.17	35.82	35.04
Orthogonal $\Delta f_{\text{nl}}/\sigma(f_{\text{nl}})$	-0.22	-0.64	-2.53	-3.06	0.36	0.16	0.30

Figure 4. The bias $\Delta f_{\rm nl}$ produced by the CIB-lensing bispectrum as a function of $\ell_{\rm max}$ for *Planck* cosmological frequencies (143 and 217 GHz). Solid lines correspond to the cleaned combined maps. Dash lines correspond to the raw map at 143 GHz and long dash lines correspond to the cleaned map at 143 GHz. Dash-and-dot lines correspond to the raw map at 217 GHz and dash-and-3-dots lines correspond to the cleaned map at 217 GHz. From left to right, we plot results for the local, equilateral and orthogonal $f_{\rm nl}$ shapes.

- (i) *Planck* raw maps per frequency

$$b_{\ell_1\ell_2\ell_3}^{(\rm CIB-Lens,\nu)} = \frac{\ell_1(\ell_1+1) - \ell_2(\ell_2+1) + \ell_3(\ell_3+1)}{2} C_{\ell_3}^{(\rm CIB-Lens,\nu)} \tilde{C}_{\ell_1}^{(\rm CMB)} b_{\ell_1}^{(\nu)} b_{\ell_2}^{(\nu)} b_{\ell_3}^{(\nu)} + (5\ perm),\tag{24}$$

$$b_{\ell_1\ell_2\ell_3}^{(\rm CMB,\nu)} = b_{\ell_1}^{(\nu)} b_{\ell_2}^{(\nu)} b_{\ell_3}^{(\nu)} b_{\ell_1\ell_2\ell_3}^{(\rm CMB)}, \qquad b_{\ell_1\ell_2\ell_3}^{(\rm ps,\nu)} = b_{\ell_1}^{(\nu)} b_{\ell_2}^{(\nu)} b_{\ell_3}^{(\nu)} b^{(\rm ps,\nu)}.\tag{25}$$

- (ii) *Planck* cleaned maps per frequency

$$b_{\ell_1\ell_2\ell_3}^{(\rm CIB-Lens,clean,\nu)} = \sum_{ijk=1}^{9} f_{\nu_i}^{(\nu)} f_{\nu_j}^{(\nu)} f_{\nu_k}^{(\nu)} b_{\ell_1}^{(\nu_i)} b_{\ell_2}^{(\nu_j)} b_{\ell_3}^{(\nu_k)} b_{\ell_1\ell_2\ell_3}^{(\rm CIB-Lens,\nu_i\nu_j\nu_k)},\tag{26}$$

$$b_{\ell_1\ell_2\ell_3}^{(\rm CMB,clean,\nu)} = \sum_{ijk=1}^{9} f_{\nu_i}^{(\nu)} f_{\nu_j}^{(\nu)} f_{\nu_k}^{(\nu)} b_{\ell_1}^{(\nu_i)} b_{\ell_2}^{(\nu_j)} b_{\ell_3}^{(\nu_k)} b_{\ell_1\ell_2\ell_3}^{(\rm CMB)}, \qquad b_{\ell_1\ell_2\ell_3}^{(\rm ps,clean,\nu)} = \sum_{ijk=1}^{9} f_{\nu_i}^{(\nu)} f_{\nu_j}^{(\nu)} f_{\nu_k}^{(\nu)} b_{\ell_1}^{(\nu_i)} b_{\ell_2}^{(\nu_j)} b_{\ell_3}^{(\nu_k)} b^{(\rm ps,\nu_i,\nu_j,\nu_k)}.\tag{27}$$

- (iii) *Planck* combined cleaned maps

$$b_{\ell_1\ell_2\ell_3}^{(\rm CIB-Lens,comb)} = \sum_{ijk=1}^{9} g_{\ell_1}^{(\nu_i)} g_{\ell_2}^{(\nu_j)} g_{\ell_3}^{(\nu_k)} b_{\ell_1}^{(\nu_i)} b_{\ell_2}^{(\nu_j)} b_{\ell_3}^{(\nu_k)} b_{\ell_1\ell_2\ell_3}^{(\rm CIB-Lens,\nu_i\nu_j\nu_k)},\tag{28}$$

$$b_{\ell_1\ell_2\ell_3}^{(\rm CMB,comb)} = \sum_{ijk=1}^{9} g_{\ell_1}^{(\nu_i)} g_{\ell_2}^{(\nu_j)} g_{\ell_3}^{(\nu_k)} b_{\ell_1}^{(\nu_i)} b_{\ell_2}^{(\nu_j)} b_{\ell_3}^{(\nu_k)} b_{\ell_1\ell_2\ell_3}^{(\rm CMB)}, \qquad b_{\ell_1\ell_2\ell_3}^{(\rm ps,comb)} = \sum_{ijk=1}^{9} g_{\ell_1}^{(\nu_i)} g_{\ell_2}^{(\nu_j)} g_{\ell_3}^{(\nu_k)} b_{\ell_1}^{(\nu_i)} b_{\ell_2}^{(\nu_j)} b_{\ell_3}^{(\nu_k)} b^{(\rm ps,\nu_i,\nu_j,\nu_k)}.\tag{29}$$

$b_{\ell_1\ell_2\ell_3}^{(\rm CMB)}$ is the primordial bispectrum (see e.g. Curto et al. 2013, for the equations for the local, equilateral and orthogonal shapes). The term $b_{\ell_1\ell_2\ell_3}^{(\rm CIB-Lens,\nu_i\nu_j\nu_k)}$ can be straightforwardly computed as a generalisation of the CIB-lensing bispectrum in Eq. (16) for three different frequencies

$$
\begin{aligned}
b_{\ell_1\ell_2\ell_3}^{(\rm CIB-Lens,\nu_i\nu_j\nu_k)} &\equiv \frac{\ell_1(\ell_1+1)-\ell_2(\ell_2+1)+\ell_3(\ell_3+1)}{2} C_{\ell_3}^{(\rm CIB-Lens,\nu_k)} \tilde{C}_{\ell_1}^{(\rm CMB)} + \frac{\ell_1(\ell_1+1)-\ell_3(\ell_3+1)+\ell_2(\ell_2+1)}{2} C_{\ell_2}^{(\rm CIB-Lens,\nu_j)} \tilde{C}_{\ell_1}^{(\rm CMB)} \\
&+ \frac{\ell_2(\ell_2+1)-\ell_1(\ell_1+1)+\ell_3(\ell_3+1)}{2} C_{\ell_3}^{(\rm CIB-Lens,\nu_k)} \tilde{C}_{\ell_2}^{(\rm CMB)} + \frac{\ell_3(\ell_3+1)-\ell_1(\ell_1+1)+\ell_2(\ell_2+1)}{2} C_{\ell_2}^{(\rm CIB-Lens,\nu_j)} \tilde{C}_{\ell_3}^{(\rm CMB)} \\
&+ \frac{\ell_2(\ell_2+1)-\ell_3(\ell_3+1)+\ell_1(\ell_1+1)}{2} C_{\ell_1}^{(\rm CIB-Lens,\nu_i)} \tilde{C}_{\ell_2}^{(\rm CMB)} + \frac{\ell_3(\ell_3+1)-\ell_2(\ell_2+1)+\ell_1(\ell_1+1)}{2} C_{\ell_1}^{(\rm CIB-Lens,\nu_i)} \tilde{C}_{\ell_3}^{(\rm CMB)}.
\end{aligned}\tag{30}
$$

Finally, the total point sources bispectrum $b_{\ell_1\ell_2\ell_3}^{(\rm ps,\nu_i,\nu_j,\nu_k)}$ is computed from the standard prescription in terms of radio and CIB shot noise bispectra (see Appendix C for details on how we estimate shot noise bispectra of point sources when multiple frequencies are considered)

$$b_{\ell_1\ell_2\ell_3}^{(\rm ps,\nu_i,\nu_j,\nu_k)} = b_{\rm sn}^{(\rm Radio,\nu_i,\nu_j,\nu_k)} + b_{\rm sn}^{(\rm CIB,\nu_i,\nu_j,\nu_k)} \sqrt{\frac{C_{\ell_1}^{(\rm CIB,\nu_i)} C_{\ell_2}^{(\rm CIB,\nu_j)} C_{\ell_3}^{(\rm CIB,\nu_k)}}{C_{\rm sn}^{(\rm CIB,\nu_i)} C_{\rm sn}^{(\rm CIB,\nu_j)} C_{\rm sn}^{(\rm CIB,\nu_k)}}}.\tag{31}$$

Considering weak levels of non-Gaussianity, the bias induced in the primordial non-Gaussianity $f_{\rm nl}$ due to a given target bispectrum $B^{(\tt targ)}_{\ell_1\ell_2\ell_3}$ is given by (see e.g. Lewis et al. 2011; Lacasa et al. 2012):

$$\Delta f_{\rm nl} = \sigma^2\left(f_{\rm nl}\right) \times \sum_{\ell_1 \leqslant \ell_2 \leqslant \ell_3}^{\ell_{\rm max}} \frac{b^{(\tt targ)}_{\ell_1\ell_2\ell_3} b^{(\tt prim)}_{\ell_1\ell_2\ell_3}}{\sigma^2\left(b^{(\tt obs)}_{\ell_1\ell_2\ell_3}\right)}, \tag{32}$$

where $\sigma^2\left(b^{(\tt obs)}_{\ell_1\ell_2\ell_3}\right)$ is the variance of the total observed bispectrum (Komatsu & Spergel 2001)

$$\sigma^2\left(b^{(\tt obs)}_{\ell_1\ell_2\ell_3}\right) \equiv \langle b^{(\tt obs)}_{\ell_1\ell_2\ell_3} b^{(\tt obs)}_{\ell_1\ell_2\ell_3}\rangle - \langle b^{(\tt obs)}_{\ell_1\ell_2\ell_3}\rangle\langle b^{(\tt obs)}_{\ell_1\ell_2\ell_3}\rangle \simeq \frac{1}{I^2_{\ell_1\ell_2\ell_3}} \Delta_{\ell_1\ell_2\ell_3} C_{\ell_1} C_{\ell_2} C_{\ell_3}, \tag{33}$$

$$\Delta_{\ell_1\ell_2\ell_3} = 1 + 2\delta_{\ell_1\ell_2}\delta_{\ell_2\ell_3} + \delta_{\ell_1\ell_2} + \delta_{\ell_2\ell_3} + \delta_{\ell_1\ell_3}, \tag{34}$$

C_ℓ is the total power spectrum of the map including CMB, CIB, radio sources and instrumental noise spectra and

$$I_{\ell_1\ell_2\ell_3} \equiv \sqrt{\frac{(2\ell_1+1)(2\ell_2+1)(2\ell_3+1)}{4\pi}} \begin{pmatrix} \ell_1 & \ell_2 & \ell_3 \\ 0 & 0 & 0 \end{pmatrix}. \tag{35}$$

Finally $\sigma^2\left(f_{\rm nl}\right)$ is the expected variance of the $f_{\rm nl}$ parameter, given in terms of its Fisher matrix

$$\sigma^{-2}\left(f_{\rm nl}\right) = \sum_{\ell_1 \leqslant \ell_2 \leqslant \ell_3}^{\ell_{\rm max}} \frac{\left(b^{(\tt prim)}_{\ell_1\ell_2\ell_3} I_{\ell_1\ell_2\ell_3}\right)^2}{\sigma^2\left(b^{(\tt obs)}_{\ell_1\ell_2\ell_3}\right)}. \tag{36}$$

The values of $\sigma^2\left(f_{\rm nl}\right)$ for the different maps are given in Table 3. For the SEVEM combined map they agree well with the values published by Planck 2013 results XXIV (2014)[6]. Note that at 143 and 217 GHz, the component separation technique slightly increases the error on $f_{\rm nl}$. This is due to the extra noise added by the template subtraction and it might be seen as the price to pay to have CMB cleaned maps.

3.3 $f_{\rm nl}$ bias due to CIB–lensing and extragalactic sources bispectra

The bias $\Delta f_{\rm nl}$ induced by the CIB-lensing correlation and unresolved extragalactic sources is estimated for the three types of maps previously described and for the local, equilateral and orthogonal $f_{\rm nl}$ shapes in the frequency range between 100 and 353 GHz. Results are presented in Table 3 and Figure 4 for the CIB-lensing, and Table 4 and Figure 5 for the unresolved extragalactic sources.

For the frequency range considered here, the CIB-lensing bispectrum causes negligible bias in the primordial local and equilateral shapes with respect to the uncertainty on $f_{\rm nl}$ estimated by Eq. (36). The bias is also negligible for the orthogonal shape in the 100 and 143 GHz raw maps but reaches 2 and 3 σ detection levels for the 217 and 353 GHz raw maps respectively. The orthogonal bias is again negligible for the foreground-reduced maps at 143 and 217 GHz and the combined map (see Table 3 and Fig. 4). These results are explained as follows. Regarding the local shape, the CMB primordial signal peaks in squeezed configurations, such as $(\ell_1, \ell_2, \ell_3) = (1000, 1000, 2)$. However in this regime, the CIB-lensing bispectrum loses most of its amplitude (see top-left panel of Fig. 2). Regarding the equilateral shape, the CMB primordial signal is spread in configurations such that $\ell_1 = \ell_2 = \ell_3 = \ell$ and becomes strongest at high resolution. The CIB-lensing bispectrum has some peaks in equilateral configurations (see bottom-left panel of Fig. 2) but they are located at low ℓ and therefore they do not significantly couple with the CMB primordial equilateral signal. Finally regarding the orthogonal shape, the CMB primordial signal is peaked in configurations such as $\ell_2 = \ell_3 = 2\ell_1$ and $\ell_2 = \ell_3 = \ell_1$ (Martínez-González & Planck Collaboration 2012). They couple with the CIB-lensing signal producing an increasing bias for multipoles $\ell > 500$ (see Fig. 4). This explains the bias predicted for the raw channels at high frequency. The process of cleaning through the component separation subtracts part of the CIB signal and the bias for this shape is reduced in cleaned maps to about 30 per cent of the *Planck* uncertainty.

The unresolved extragalactic sources present levels of detection greater than 2σ at 353 GHz for the local, equilateral and orthogonal shapes due to the higher amplitude of IR sources at this frequency. There is a 2σ detection at 100 GHz for the equilateral shape which can be explained as a trace of the radio sources. The bias is again negligible for the foreground-reduced maps as the component separation technique is able to significantly reduce their contamination (see Table 4 and Fig. 5). These results are well in agreement with previous analyses from Lacasa et al. (2012) and Curto et al. (2013). These results are explained as follows. Regarding the local shape, the bispectrum of extragalactic sources does not have a significant signal in squeezed configurations at low frequencies (see top-left panel of Fig. 2) and therefore there we do not expected significant correlations with the CMB primordial local bispectrum. However the high frequency channels contain a significant contribution from IR sources in squeezed configurations that couple with the local CMB bispectrum. Regarding the equilateral shape, the extragalactic radio sources have significant signal in equilateral configurations ($\ell_1 = \ell_2 = \ell_3$) at high multipoles (see bottom-left panel of Fig. 2) explaining the deviation seen in Table 4. The bispectrum of IR sources is dominant in equilateral configurations and at high multipoles explaining the large bias predicted at 353 GHz. Finally regarding the orthogonal shape, only the high frequency IR source bispectrum has a strong signal in configurations that couple with the CMB primordial orthogonal bispectrum, especially for high multipoles, explaining the large bias predicted at 353 GHz.

---

[6] During the process of publication of this article the Planck Collaboration published new scientific results, in particular the first results on f_{nl} with temperature and polarisation maps (Planck 2015 results XIX 2015). No significant changes have been reported in the new Planck article regarding the results with temperature only.
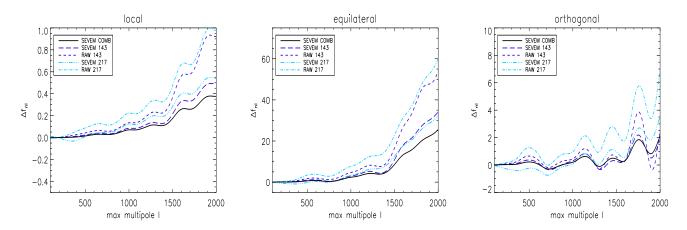
Figure 5. The bias Δf_{nl} produced by the point sources bispectrum as a function of $\ell_{\max}$ for *Planck* cosmological frequencies (143 and 217 GHz). Solid lines correspond to the cleaned combined maps. Dash lines correspond to the raw map at 143 GHz and long dash lines correspond to the cleaned map at 143 GHz. Dash-and-dot lines correspond to the raw map at 217 GHz and dash-and-3-dots lines correspond to the cleaned map at 217 GHz. From left to right, we plot results for the local, equilateral and orthogonal f_{nl} shapes.

Table 4. *Planck* expected Δf_{nl} bias due to unresolved point sources for the local, equilateral and orthogonal f_{nl} shapes for $\ell_{\max} = 2000$.

Frequency (GHz)	100	143	217	353	SEVEM 143	SEVEM 217	SEVEM combined
Local Δf_{nl}	2.95	0.92	0.98	29.30	0.50	0.54	0.35
Local $\Delta f_{\mathrm{nl}}/\sigma(f_{\mathrm{nl}})$	0.44	0.18	0.18	2.08	0.09	0.09	0.07
Equilateral Δf_{nl}	160.07	54.20	60.32	1648.70	34.19	32.36	30.38
Equilateral $\Delta f_{\mathrm{nl}}/\sigma(f_{\mathrm{nl}})$	2.10	0.79	0.85	12.25	0.48	0.45	0.45
Orthogonal Δf_{nl}	10.53	2.45	7.00	553.01	1.87	3.56	2.94
Orthogonal $\Delta f_{\mathrm{nl}}/\sigma(f_{\mathrm{nl}})$	0.27	0.07	0.20	7.24	0.05	0.10	0.09

4 DETECTABILITY OF THE CIB–LENSING BISPECTRUM

In this section we develop statistical tools to detect the CIB–lensing bispectrum using an alternative approach to the widely known technique based on the cross-correlation of lensing potential reconstruction and temperature maps used for example in Planck 2013 results XVIII (2014) and Planck 2013 results XIX (2014). The cross-correlation approach followed in these publications used a lensing reconstruction based on quadratic combination of *Planck* CMB maps (Planck 2013 results XVII 2014). The estimators that we propose in this article are directly defined in terms of cubic combinations of *Planck* maps where the CMB signal is dominant (100 to 217 GHz) and *Planck* maps where the CIB signal is dominant (217 to 857 GHz). Both approaches are linearly dependent and should result in similar levels of efficiency to detect the targeted CIB–lensing signal. The advantage of the new approach defined here is the application for the first time of a battery of well-known, efficient and optimal estimators widely used in the primordial bispectrum estimation to detect the CIB–lensing bispectrum. This approach has already been applied to the ISW–lensing estimation by Mangilli et al. (2013).

4.1 Single frequency bispectrum estimator

The optimal estimator for the amplitude of the CIB–lensing bispectrum, assuming small departures of non-Gaussianity, for the ideal, full–sky and isotropic instrumental noise is

$$\hat{A}^{(\mathrm{CIB-Lens})} = \left(F^{-1}\right)\hat{S}^{(\mathrm{CIB-Lens})} \tag{37}$$

where

$$\hat{S}^{(\mathrm{CIB-Lens})} = \sum_{2 \leqslant \ell_1 \leqslant \ell_2 \leqslant \ell_3}^{\ell_{\max}} \frac{b^{(\mathrm{obs})}_{\ell_1 \ell_2 \ell_3} b^{(\mathrm{CIB-Lens})}_{\ell_1 \ell_2 \ell_3}}{\sigma^2\left(b^{(\mathrm{obs})}_{\ell_1 \ell_2 \ell_3}\right)}, \tag{38}$$

$$F = \sum_{2 \leqslant \ell_1 \leqslant \ell_2 \leqslant \ell_3}^{\ell_{\max}} \frac{b^{(\mathrm{CIB-Lens})}_{\ell_1 \ell_2 \ell_3} b^{(\mathrm{CIB-Lens})}_{\ell_1 \ell_2 \ell_3}}{\sigma^2\left(b^{(\mathrm{obs})}_{\ell_1 \ell_2 \ell_3}\right)}, \tag{39}$$

Table 5. Signal-to-noise ratio $\sqrt{F}$ of the amplitude of the CIB–lensing bispectrum for the *Planck* raw maps at frequencies between 100 and 857 GHz using ideal conditions (isotropic instrumental noise) from the Fisher matrix in Eq. (39) and several sky fractions available.

Frequency (GHz)	100	143	217	353	545	857
$F_{indep}^{1/2}\left(f_{sky}=1\right)$	0.55	1.80	7.57	10.19	0.25	0.00
$F_{indep}^{1/2}\left(f_{sky}=0.304\right)$	0.17	0.55	2.30	3.10	0.08	0.00
$F_{indep}^{1/2}\left(f_{sky}=0.100\right)$	0.06	0.18	0.76	1.02	0.03	0.00
$F_{joint}^{1/2}\left(f_{sky}=1\right)$	0.52	1.66	6.87	9.80	0.25	0.00
$F_{joint}^{1/2}\left(f_{sky}=0.304\right)$	0.16	0.51	2.09	2.98	0.07	0.00
$F_{joint}^{1/2}\left(f_{sky}=0.100\right)$	0.05	0.17	0.69	0.98	0.02	0.00

and the observed bispectrum $b_{\ell_1\ell_2\ell_3}^{(\mathrm{obs})}$ is based on cubic combinations of *Planck* data in the $a_{\ell m}$ decomposition on the sphere. Another interesting quantity is the expected bispectrum signal-to-noise ratio as a function of the largest scale mode $\ell_{\min}$ (Lewis et al. 2011):

$$F_{\ell_{\min}} = \sum_{\ell_{\min}\leqslant\ell_1\leqslant\ell_2\leqslant\ell_3}^{\ell_{\max}} \frac{b_{\ell_1\ell_2\ell_3}^{(\mathrm{CIB-Lens})}b_{\ell_1\ell_2\ell_3}^{(\mathrm{CIB-Lens})}}{\sigma^2\left(b_{\ell_1\ell_2\ell_3}^{(\mathrm{obs})}\right)}, \tag{40}$$

This quantity helps to find the multipole configurations where the bispectrum signal peaks.

The signal-to-noise ratio of the CIB–lensing signal of this estimator $\sqrt{F}$ is summarised in Table 5 for the frequency range between 100 and 857 GHz and $\ell_{\max} = 2000$ and different sky fractions available: 100% (full sky), 30.4%[7] and 10%. We compute this ratio considering the CIB–lensing signal alone (Eq. 39) and the joint Fisher matrix for the four non-primordial bispectra used in this article, i.e, CIB–lensing, ISW–lensing, CIB, and extragalactic point sources, by using the generalised Fisher matrix between the bispectra i and j:

$$F_{ij} = \sum_{2\leqslant\ell_1\leqslant\ell_2\leqslant\ell_3}^{\ell_{\max}} \frac{b_{\ell_1\ell_2\ell_3}^{(i)}b_{\ell_1\ell_2\ell_3}^{(j)}}{\sigma^2\left(b_{\ell_1\ell_2\ell_3}^{(\mathrm{obs})}\right)}. \tag{41}$$

The first case is simply $F_{indep} = F_{ii}$ whereas the second is $F_{joint} = 1/\left(F^{-1}\right)_{ii}$ with i being the CIB–lensing case. The significance level for the detection of the CIB–lensing signal with this estimator increases from approx. 0.5σ at 100 GHz to 9.8σ at 353 GHz considering the full sky available. In a more realistic scenario with a 10% sky available for the CIB maps, the CIB–lensing signal would be detected with a maximum precision of 1σ at 353 GHz. At higher frequencies, the CIB spectrum dominates in the denominator in Eq. (39) leading to low significance levels of detection for the CIB–lensing bispectrum.

4.2 Asymmetric estimator for CMB–CIB correlated maps

At high *Planck* frequencies the CIB bispectrum could strongly limit our capability to detect the CIB–lensing signal, as well as the ISW–lensing contribution could be a relevant "noise" at 100–217 GHz. Therefore, a more feasible procedure to detect the CIB–lensing bispectrum signal should correlate CMB signal-dominated maps and CIB signal-dominated maps. We define an estimator for the CIB-lensing signal by considering the asymmetric configuration $\tilde{a}_{\ell_1 m_1}^{(\mathrm{raw},\nu_{\mathrm{CMB}})}\tilde{a}_{\ell_2 m_2}^{(\mathrm{raw},\nu_{\mathrm{CMB}})}a_{\ell_3 m_3}^{(\mathrm{raw},\nu_{\mathrm{CIB}})}$ where ν_{CMB} and ν_{CIB} are frequency channels where the CMB and CIB signal are significant respectively. We consider $\nu_{\mathrm{CMB}} = 100$, 143 and 217 GHz and $\nu_{\mathrm{CIB}} = 217$, 353, 545 and 857 GHz. The four non-primordial averaged bispectra considered in this paper, namely the radio, CIB, CIB-lensing and ISW-lensing bispectra, are written in this asymmetric configuration by:

$$b_{\ell_1\ell_2\ell_3}^{(\mathrm{Radio})} = b_{\mathrm{sn}}^{(\mathrm{Radio},\nu_{\mathrm{CMB}},\nu_{\mathrm{CMB}},\nu_{\mathrm{CIB}})} \tag{42}$$

$$b_{\ell_1\ell_2\ell_3}^{(\mathrm{CIB})} = b_{\mathrm{sn}}^{(\mathrm{CIB},\nu_{\mathrm{CMB}},\nu_{\mathrm{CMB}},\nu_{\mathrm{CIB}})}\sqrt{\frac{C_{\ell_1}^{(\mathrm{CIB},\nu_{\mathrm{CMB}})}C_{\ell_2}^{(\mathrm{CIB},\nu_{\mathrm{CMB}})}C_{\ell_3}^{(\mathrm{CIB},\nu_{\mathrm{CIB}})}}{C_{\mathrm{sn}}^{(\mathrm{CIB},\nu_{\mathrm{CMB}})}C_{\mathrm{sn}}^{(\mathrm{CIB},\nu_{\mathrm{CMB}})}C_{\mathrm{sn}}^{(\mathrm{CIB},\nu_{\mathrm{CIB}})}}} \tag{43}$$

$$b_{\ell_1\ell_2\ell_3}^{(\mathrm{CIB-Lens})} = \left[\frac{\ell_1(\ell_1+1)-\ell_2(\ell_2+1)+\ell_3(\ell_3+1)}{2}\tilde{C}_{\ell_1}^{(\mathrm{CMB})}C_{\ell_3}^{(\mathrm{CIB-Lens},\nu_{\mathrm{CIB}})} + \frac{\ell_2(\ell_2+1)-\ell_1(\ell_1+1)+\ell_3(\ell_3+1)}{2}\tilde{C}_{\ell_2}^{(\mathrm{CMB})}C_{\ell_3}^{(\mathrm{CIB-Lens},\nu_{\mathrm{CIB}})}\right], \tag{44}$$

and

$$b_{\ell_1\ell_2\ell_3}^{(\mathrm{ISW-Lens})} = \left[\frac{\ell_1(\ell_1+1)-\ell_2(\ell_2+1)+\ell_3(\ell_3+1)}{2}\tilde{C}_{\ell_1}^{(\mathrm{CMB})}C_{\ell_3}^{(\mathrm{ISW-Lens})} + (5\,perm)\right]. \tag{45}$$

---

[7] This is the percentage of available sky used in the main results of Planck 2013 results XVIII (2014).

Table 6. The signal-to-noise ratio $\sqrt{F}$ of the amplitude of the CIB–lensing bispectrum for clean full–sky maps using the joint (Eq. 50) and independent (Eq. 52) Fisher matrices for the combinations the clean CMB at frequencies between 100 and 217 GHz and the clean CIB at frequencies between 353 and 857 GHz using 100%, (30.4%), [10%] of the sky..

Case	Frequency	$\nu_{\rm CIB} = 353$ GHz	$\nu_{\rm CIB} = 545$ GHz	$\nu_{\rm CIB} = 857$ GHz
Joint	$\nu_{\rm CMB} = 100$ GHz	42.70 (23.54) [13.50]	41.03 (22.62) [12.98]	37.60 (20.73) [11.89]
Joint	$\nu_{\rm CMB} = 143$ GHz	62.66 (34.55) [19.82]	60.15 (33.17) [19.02]	55.40 (30.54) [17.52]
Joint	$\nu_{\rm CMB} = 217$ GHz	62.37 (34.39) [19.72]	59.90 (33.03) [18.94]	55.19 (30.43) [17.45]
Independent	$\nu_{\rm CMB} = 100$ GHz	44.65 (24.62) [14.12]	43.21 (23.83) [13.66]	39.71 (21.90) [12.56]
Independent	$\nu_{\rm CMB} = 143$ GHz	68.70 (37.88) [21.73]	66.61 (36.73) [21.06]	61.42 (33.86) [19.42]
Independent	$\nu_{\rm CMB} = 217$ GHz	68.51 (37.77) [21.66]	66.42 (36.62) [21.00]	61.26 (33.78) [19.37]

The covariance matrix is nearly diagonal and can be approximated by the following expression (see Appendix D) for the CMB x CMB x CIB configurations:

$$\sigma^2\left(b_{\ell_1 \ell_2 \ell_3}^{(\rm obs)}\right) = \frac{1}{I_{\ell_1 \ell_2 \ell_3}^2} \tilde{C}_{\ell_1}^{(\rm CMB)} \tilde{C}_{\ell_2}^{(\rm CMB)} C_{\ell_3}^{(\rm CIB)} \left(1 + \delta_{\ell_1 \ell_2}\right). \tag{46}$$

The CIB-lensing estimator for this configuration is now:

$$\hat{S}^{(\rm CIB-Lens)} = \sum_{2 \leqslant \ell_1 \leqslant \ell_2, \ell_3}^{\ell_{\rm max}} \frac{b_{\ell_1 \ell_2 \ell_3}^{(\rm obs)} b_{\ell_1 \ell_2 \ell_3}^{(\rm CIB-Lens)}}{\sigma^2\left(b_{\ell_1 \ell_2 \ell_3}^{(\rm obs)}\right)}. \tag{47}$$

The estimator is different with respect to the single map estimators since it admits more configurations because we just have symmetry under permutations of ℓ_1 and ℓ_2 whereas ℓ_3 is free. The Fisher matrix for the four bispectra considered in this work is defined as (Komatsu & Spergel 2001):

$$F_{ij} = \sum_{2 \leqslant \ell_1 \leqslant \ell_2, \ell_3}^{\ell_{\rm max}} \frac{b_{\ell_1 \ell_2 \ell_3}^{(i)} b_{\ell_1 \ell_2 \ell_3}^{(j)}}{\sigma^2\left(b_{\ell_1 \ell_2 \ell_3}^{(\rm obs)}\right)} \tag{48}$$

where the indices i and j cover the following bispectra: (1) radio, (2) CIB, (3) CIB-lensing and (4) ISW-lensing. We also define the Fisher matrix in terms of the minimum multipole $\ell_{\rm min}$:

$$\left(F_{ij}\right)_{\ell_{\rm min}} = \sum_{\ell_{\rm min} \leqslant \ell_1 \leqslant \ell_2, \ell_3}^{\ell_{\rm max}} \frac{b_{\ell_1 \ell_2 \ell_3}^{(i)} b_{\ell_1 \ell_2 \ell_3}^{(j)}}{\sigma^2\left(b_{\ell_1 \ell_2 \ell_3}^{(\rm obs)}\right)}. \tag{49}$$

The Cramér-Rao inequality states that the inverse of the Fisher information matrix is a lower bound on the variance of any unbiased estimator in the best optimal conditions. Therefore the variance of the amplitude of each bispectra can be obtained by inverting the Fisher matrix

$$\sigma_{\rm joint}^2(A_i) = \left(F^{-1}\right)_{ii}. \tag{50}$$

This approach performs a joint analysis including the correlations among the four types of bispectra, in comparison to the independent constraint that would have a lower variance:
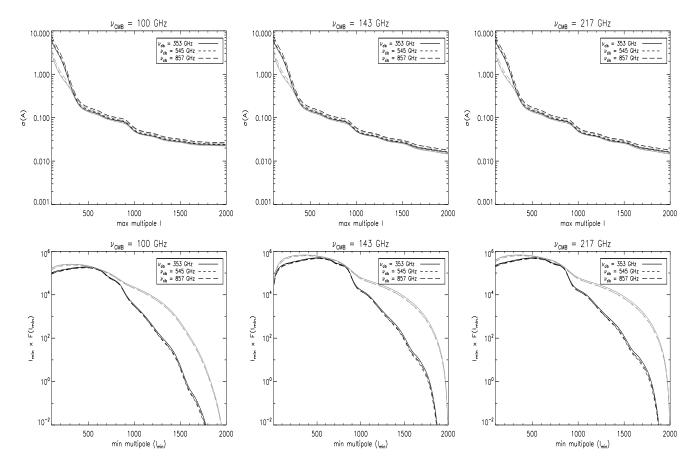
$$\sigma_{\rm indep}^2(A_i) = (F_{ii})^{-1}. \tag{51}$$

The signal-to-noise ratio is given by:

$$F_{\rm indep}^{1/2}(A_i) = F_{ii}^{1/2} \qquad F_{\rm joint}^{1/2}(A_i) = 1/\sqrt{\left(F^{-1}\right)_{ii}}. \tag{52}$$

The expected uncertainties for the CIB-lensing estimator, computed both using the independent and the joint approach, are plotted in Fig. 6 and is summarised in Table 6 for $\ell_{\rm max} = 2000$. In an ideal scenario where the CMB and the CIB maps are completely separated in two full sky maps, we would have a detectability level of approximately 63σ in the best configurations given in Table 6 for $\ell_{\rm max} = 2000$. However available CIB maps cover only about 10% of the sky (Planck 2013 results XXX 2014) in the best case scenarios. For the incomplete sky case, the detectability level of the bispectrum is rescaled by the fraction of the available sky $f_{\rm sky}$ such that $\sigma(A) \longrightarrow \sigma(A)/\sqrt{f_{\rm sky}}$. As the CIB–lensing bispectrum is not squeezed (see Fig. 6), this case is not affected by the loss of low multipoles, which are unobservable for small sky fractions, so this approximation is safe up to the mentioned 10% of the sky. This would provide detectability levels between 12σ to 20σ respectively for a mask with 10% of the sky available using the joint estimator (see Table 6).

We have compared our results with the estimates of the CIB–lensing correlation published in Planck 2013 results XVIII (2014). The statistical estimator used in that work is based on a cross-correlation between the lensing potential in harmonic space, $\phi_{\ell m}$, and a temperature map. The amplitude of the detection is obtained with the quadrature sum of the significance of the different multipole bins. This amplitude takes into account effects such as correlations among different bins but no systematic errors or point source corrections. The final estimates presented in that paper are computed using the lensing reconstruction at 143 GHz and the *Planck* HFI foreground reduced maps with a mask of 30.4% of available sky. The results obtained in this way and our predictions for the same configuration are given in Table 7.

Figure 6. *Top:* the uncertainty for the CIB–lensing bispectrum amplitude $\sigma(A)$ as a function of $\ell_{\max}$ for cleaned CMB maps (at 100, 143 and 217 GHz) combined with CIB dominated maps at 353, 545 and 857 GHz using the independent estimates (grey lines) and using the joint estimates (black lines). *Bottom:* the Fischer matrix $F_{\ell_{\min}}$ (multiplied by $\ell_{\min}$) as a function of $\ell_{\min}$ for the same cases as above.

Table 7. Significance of the amplitude of the CIB–lensing correlation using the lensing reconstruction at 143 GHz and the *Planck* HFI foreground reduced maps with a mask of 30.4% of available sky. *Top line:* measurements by Planck 2013 results XVIII (2014). *Bottom line:* our predictions for an optimal bispectrum estimator for the same configuration.

Case	$\nu_{\mathrm{CIB}} = 353$ GHz	$\nu_{\mathrm{CIB}} = 545$ GHz	$\nu_{\mathrm{CIB}} = 857$ GHz
Number of standard deviations[a] (Planck 2013 results XVIII 2014)	31 (24)	42 (19)	32 (16)
$\sqrt{F}$	35	33	31

[a] Statistical error and statistical plus systematic errors in parenthesis.

Planck 2013 results XVIII (2014) provides two types of detection significances: one that only includes the statistical errors only and another one that includes statistical and systematic errors. Compared to the first one – as we do not consider systematic errors here – the detection significance by Planck 2013 results XVIII (2014) and our model are nearly equivalent for the 353 to 857 GHz range. Note that the values measured by Planck 2013 results XVIII (2014) are quite sensitive to the systematic effects (see Table 7). We have additionally repeated our analysis without adding instrumental noise, i.e. for ideal conditions, and have found $\sqrt{F} = 39, 38, 35$ for the 353, 545 and 857 GHz bands. Both cases show a decreasing trend in the signal-to-noise level of the CIB-lensing correlation as we increase the frequency, due to the higher contamination of the CIB. We do not see a peak at 545 GHz, and we think that the peak observed in Planck 2013 results XVIII (2014) at 545 GHz might be explained by an unknown systematic artefact present in the data.

The Wick expansions, used to compute the variance of the observed bispectra (see Appendix D), are good approximations when the departures from non-Gaussianity are limited. Therefore, we could expect some contributions to the covariance matrix of the bispectrum in Eq. (46) due to higher order moments (see Section 4.3 in Planck 2013 results XXX 2014). We have computed higher order contributions to the variance in Appendix D. The result is that higher order moments do not add a significant contribution to the covariance and that the Wick expansions used in this paper hold.

5 KSW-BASED ESTIMATORS FOR THE CIB-LENSING BISPECTRUM

We present the formalism of an optimal estimator for the amplitude of the bispectrum induced by the CIB–lensing correlation, based on the estimator developed by Komatsu et al. (2005, KSW) for the primordial non-Gaussianity and extended to the ISW–lensing bispectrum by Mangilli et al. (2013). Here we consider the ideal case without noise and beam function. The case of a realistic experiment can be straightforward extended (see, e.g., Lacasa & Aghanim 2012; Mangilli et al. 2013).

5.1 Single frequency bispectrum estimator

The optimal estimator $\hat{S}$ of the CIB–lensing bispectrum for a single frequency map is given by Eq. (38). Using the identity

$$\sum_{\ell_1 \leqslant \ell_2 \leqslant \ell_3}^{\ell_{\max}} F_{\ell_1 \ell_2 \ell_3} = \frac{1}{6} \sum_{\ell_1 \ell_2 \ell_3}^{\ell_{\max}} F_{\ell_1 \ell_2 \ell_3} \Delta_{\ell_1 \ell_2 \ell_3} \tag{53}$$

for any given $F_{\ell_1 \ell_2 \ell_3}$ symmetric in ℓ_1, ℓ_2, ℓ_3, we can write the estimator $\hat{S}$ as:

$$
\begin{aligned}
\hat{S}^{\text{CIB}-\text{Lens}} &= \frac{1}{6} \sum_{\ell_1 \ell_2 \ell_3} \sum_{m_1 m_2 m_3} \begin{pmatrix} \ell_1 & \ell_2 & \ell_3 \\ m_1 & m_2 & m_3 \end{pmatrix} \frac{a_{\ell_1 m_1} a_{\ell_2 m_2} a_{\ell_3 m_3}}{C_{\ell_1} C_{\ell_2} C_{\ell_3}} \sqrt{\frac{(2\ell_1+1)(2\ell_2+1)(2\ell_3+1)}{4\pi}} \begin{pmatrix} \ell_1 & \ell_2 & \ell_3 \\ 0 & 0 & 0 \end{pmatrix} b_{\ell_1 \ell_2 \ell_3}^{(\text{CIB}-\text{Lens})} \\
&= \frac{1}{6} \int d^2 \hat{\mathbf{n}} \sum_{\ell_1 \ell_2 \ell_3} \sum_{m_1 m_2 m_3} \frac{a_{\ell_1 m_1} a_{\ell_2 m_2} a_{\ell_3 m_3}}{C_{\ell_1} C_{\ell_2} C_{\ell_3}} Y_{\ell_1 m_1}(\hat{\mathbf{n}}) Y_{\ell_2 m_2}(\hat{\mathbf{n}}) Y_{\ell_3 m_3}(\hat{\mathbf{n}}) b_{\ell_1 \ell_2 \ell_3}^{(\text{CIB}-\text{Lens})}
\end{aligned} \tag{54}
$$

where C_ℓ is the total power spectrum in the single frequency map. By including the bispectrum formula (Eq. 16) into Eq. (54) and factorizing the ℓ dependence, the integral becomes

$$
\begin{aligned}
\hat{S}^{\text{CIB}-\text{Lens}} = \frac{1}{12} \int d^2 \hat{\mathbf{n}} \sum_{\ell_1 \ell_2 \ell_3} \sum_{m_1 m_2 m_3} \Bigg\{ &\left[\ell_1(\ell_1+1) a_{\ell_1 m_1} Y_{\ell_1 m_1}(\hat{\mathbf{n}}) \frac{\tilde{C}_{\ell_1}^{\text{CMB}}}{C_{\ell_1}} \right] \left[\frac{a_{\ell_2 m_2} Y_{\ell_2 m_2}(\hat{\mathbf{n}})}{C_{\ell_2}} \right] \left[a_{\ell_3 m_3} Y_{\ell_3 m_3}(\hat{\mathbf{n}}) \frac{C_{\ell_3}^{(\text{CIB}-\text{Lens})}}{C_{\ell_3}} \right] \\
&- \left[a_{\ell_1 m_1} Y_{\ell_1 m_1}(\hat{\mathbf{n}}) \frac{\tilde{C}_{\ell_1}^{\text{CMB}}}{C_{\ell_1}} \right] \left[\ell_2(\ell_2+1) \frac{a_{\ell_2 m_2} Y_{\ell_2 m_2}(\hat{\mathbf{n}})}{C_{\ell_2}} \right] \left[a_{\ell_3 m_3} Y_{\ell_3 m_3}(\hat{\mathbf{n}}) \frac{C_{\ell_3}^{(\text{CIB}-\text{Lens})}}{C_{\ell_3}} \right] \\
&+ \left[a_{\ell_1 m_1} Y_{\ell_1 m_1}(\hat{\mathbf{n}}) \frac{\tilde{C}_{\ell_1}^{\text{CMB}}}{C_{\ell_1}} \right] \left[\frac{a_{\ell_2 m_2} Y_{\ell_2 m_2}(\hat{\mathbf{n}})}{C_{\ell_2}} \right] \left[\ell_3(\ell_3+1) a_{\ell_3 m_3} Y_{\ell_3 m_3}(\hat{\mathbf{n}}) \frac{C_{\ell_3}^{(\text{CIB}-\text{Lens})}}{C_{\ell_3}} \right] + 5 perm. \Bigg\}.
\end{aligned} \tag{55}
$$

Now, if we define the following filtered maps

$$P(\hat{\mathbf{n}}) \equiv \sum_{\ell m} a_{\ell m} Y_{\ell m}(\hat{\mathbf{n}}) \frac{\tilde{C}_\ell^{(\text{CMB})}}{C_\ell} \qquad Q(\hat{\mathbf{n}}) \equiv \sum_{\ell m} a_{\ell m} Y_{\ell m}(\hat{\mathbf{n}}) \frac{C_\ell^{(\text{CIB}-\text{Lens})}}{C_\ell} \qquad E(\hat{\mathbf{n}}) \equiv \sum_{\ell m} \frac{a_{\ell m} Y_{\ell m}(\hat{\mathbf{n}})}{C_\ell}, \tag{56}$$

with the corresponding $\delta^2 X$ maps (with $X = P, Q, E$) obtained by substituting $a_{\ell m}$ with $\ell(\ell+1) a_{\ell m}$, Eq. (55) becomes

$$\hat{S}^{\text{CIB}-\text{Lens}} = \frac{1}{2} \int d^2 \hat{\mathbf{n}} \left[\delta^2 P(\hat{\mathbf{n}}) E(\hat{\mathbf{n}}) Q(\hat{\mathbf{n}}) - P(\hat{\mathbf{n}}) \delta^2 E(\hat{\mathbf{n}}) Q(\hat{\mathbf{n}}) + P(\hat{\mathbf{n}}) E(\hat{\mathbf{n}}) \delta^2 Q(\hat{\mathbf{n}}) \right]. \tag{57}$$

The expressions in this section assume that the full inverse covariance matrix can be replaced by a diagonal covariance term, $(C^{-1}a)_{\ell m} \to a_{\ell m}/C_\ell$. In a real experiment, this approximation might not be valid. In fact, we have to take into account that clean CIB maps can be obtained only in small areas of the sky due to the Galactic dust contamination. Here we are using this approximation just for simplicity. Moreover, when rotational invariance is broken by, e.g., a Galactic mask or an anisotropic noise, a linear term should be subtracted from the estimator in Eq. (54) (see, e.g. Mangilli et al. 2013). This linear term correction for a generic bispectrum shape $b_{\ell_1 \ell_2 \ell_3}$ is given by:

$$\hat{S}_{lin} = -\frac{1}{2} \int d^2 \hat{n} \sum_{\ell m} b_{\ell_1 \ell_2 \ell_3} \frac{a_{\ell_3 m_3}}{C_{\ell_1} C_{\ell_2} C_{\ell_3}} Y_{\ell_1 m_1}(\hat{n}) Y_{\ell_2 m_2}(\hat{n}) Y_{\ell_3 m_3}(\hat{n}). \tag{58}$$

Using the explicit form of the CIB–lensing bispectrum, the linear term correction for the single-frequency CIB–lensing estimator defined in Eq. (57) is given by:

$$
\begin{aligned}
S_{lin}^{\text{CIB}-\text{Lens}} = \; &- \frac{1}{2} \int d^2 \hat{n} \Big\{ Q(\hat{n}) \left[\langle P(\hat{n}) \delta^2 E(\hat{n}) \rangle - \langle E(\hat{n}) \delta^2 P(\hat{n}) \rangle \right] - \delta^2 Q(\hat{n}) \langle P(\hat{n}) E(\hat{n}) \rangle - E(\hat{n}) \left[\langle Q(\hat{n}) \delta^2 P(\hat{n}) \rangle - \langle P(\hat{n}) \delta^2 Q(\hat{n}) \rangle \right] \\
&+ \delta^2 E(\hat{n}) \langle P(\hat{n}) Q(\hat{n}) \rangle - \delta^2 P(\hat{n}) \langle E(\hat{n}) Q(\hat{n}) \rangle + P(\hat{n}) \left[\langle Q(\hat{n}) \delta^2 E(\hat{n}) \rangle - \langle E(\hat{n}) \delta^2 Q(\hat{n}) \rangle \right] \Big\}.
\end{aligned} \tag{59}
$$

The averages in Eq. (59) correspond to realistic Monte Carlo simulations which contain the instrumental properties (beams, noise, masks) and also the type of non-Gaussianity we are testing (in this case the CIB–lensing).

In the above treatment we have also supposed that the CIB–lensing term is the only relevant non–Gaussian contribution. This is of course not the case when a single frequency map is used. In fact, the bispectrum from CIB sources and from ISW–lensing correlation can give stronger contributions as shown in Fig. 2. A joint estimation of their amplitude can be applied (see Lacasa & Aghanim 2012) using estimators developed considering only one source of non–Gaussianity.

5.2 Asymmetric estimator for CMB–CIB correlated maps

The estimator for CMB–CIB correlated maps is defined in Eq. (47). If we indicate the lensed CMB map and the CIB map at frequency ν as

$$\left(\frac{\Delta T}{T}\right)^{(\text{CMB})}(\hat{\mathbf{n}}) = \sum_{\ell m} \tilde{a}_{\ell m}^{(\text{CMB})} Y_{\ell m}(\hat{\mathbf{n}}) \qquad T_{\nu}^{(\text{CIB})}(\hat{\mathbf{n}}) = \sum_{\ell m} a_{\ell m}^{(\text{CIB})} Y_{\ell m}(\hat{\mathbf{n}}), \tag{60}$$

the estimator in Eq. (47) becomes now:

$$\hat{S}^{\text{CIB}-\text{Lens}*} = \frac{1}{2} \sum_{\ell_1 \ell_2 \ell_3} \sum_{m_1 m_2 m_3} G_{m_1 m_2 m_3}^{\ell_1 \ell_2 \ell_3} \frac{\tilde{a}_{\ell_1 m_1}^{(\text{CMB})} \tilde{a}_{\ell_2 m_2}^{(\text{CMB})} a_{\ell_3 m_3}^{(\text{CIB})}}{\tilde{C}_{\ell_1}^{(\text{CMB})} \tilde{C}_{\ell_2}^{(\text{CMB})} C_{\ell_3}^{(\text{CIB})}} b_{\ell_1 \ell_2 \ell_3}^{(\text{CIB}-\text{Lens})*}, \tag{61}$$

where here the CIB–lensing bispectrum includes only two permutations

$$b_{\ell_1 \ell_2 \ell_3}^{(\text{CIB}-\text{Lens})*} = \frac{\ell_1(\ell_1+1) - \ell_2(\ell_2+1) + \ell_3(\ell_3+1)}{2} \tilde{C}_{\ell_1}^{(\text{CMB})} C_{\ell_3}^{(\text{CIB}-\text{Lens})} + \frac{\ell_2(\ell_2+1) - \ell_1(\ell_1+1) + \ell_3(\ell_3+1)}{2} \tilde{C}_{\ell_2}^{(\text{CMB})} C_{\ell_3}^{(\text{CIB}-\text{Lens})}. \tag{62}$$

The factor $1/2$ in Eq. (61) is due to the fact the bispectrum is now symmetric only in ℓ_1 and ℓ_2 and $\sum_{\ell_1 \leqslant \ell_2, \ell_3} \longrightarrow \frac{1}{2} \sum_{\ell_1 \ell_2 \ell_3}(1 + \delta_{\ell_1 \ell_2})$. By defining new filtered maps as:

$$P_{\text{CMB}}(\hat{\mathbf{n}}) \equiv \left(\frac{\Delta T}{T}\right)^{(\text{CMB})}(\hat{\mathbf{n}}) = \sum_{\ell m} \tilde{a}_{\ell m}^{(\text{CMB})} Y_{\ell m}(\hat{\mathbf{n}}) \quad Q_{\text{CIB}}(\hat{\mathbf{n}}) \equiv \sum_{\ell m} a_{\ell m}^{(\text{CIB})} Y_{\ell m}(\hat{\mathbf{n}}) \frac{C_{\ell}^{(\text{CIB}-\text{Lens})}}{C_{\ell}^{(\text{CIB})}} \quad E_{\text{CMB}}(\hat{\mathbf{n}}) \equiv \sum_{\ell m} \frac{\tilde{a}_{\ell m}^{(\text{CMB})} Y_{\ell m}(\hat{\mathbf{n}})}{\tilde{C}_{\ell}^{(\text{CMB})}}. \tag{63}$$

the estimator can be written in terms of filtered maps as:

$$\hat{S}^{\text{CIB}-\text{Lens}*} = -\frac{1}{2} \int d^2\hat{\mathbf{n}} \left[\delta^2 P_{\text{CMB}}(\hat{\mathbf{n}}) E_{\text{CMB}}(\hat{\mathbf{n}}) Q_{\text{CIB}}(\hat{\mathbf{n}}) - P_{\text{CMB}}(\hat{\mathbf{n}}) \delta^2 E_{\text{CMB}}(\hat{\mathbf{n}}) Q_{\text{CIB}}(\hat{\mathbf{n}}) + P_{\text{CMB}}(\hat{\mathbf{n}}) E_{\text{CMB}}(\hat{\mathbf{n}}) \delta^2 Q_{\text{CIB}}(\hat{\mathbf{n}}) \right]. \tag{64}$$

The linear term correction of this estimator can be straightforwardly computed following the same steps already developed for the single-frequency estimator:

$$
\begin{aligned}
S_{lin}^{\text{CIB}-\text{Lens}*} =& \\
-& \frac{1}{2} \int d^2\hat{n} \Big\{ Q_{\text{CIB}}(\hat{n}) \Big[\langle P_{\text{CMB}}(\hat{n}) \delta^2 E_{\text{CMB}}(\hat{n}) \rangle - \langle E_{\text{CMB}}(\hat{n}) \delta^2 P_{\text{CMB}}(\hat{n}) \rangle \Big] - \delta^2 Q_{\text{CIB}}(\hat{n}) \langle P_{\text{CMB}}(\hat{n}) E_{\text{CMB}}(\hat{n}) \rangle \\
-& E_{\text{CMB}}(\hat{n}) \Big[\langle Q_{\text{CIB}}(\hat{n}) \delta^2 P_{\text{CMB}}(\hat{n}) \rangle - \langle P_{\text{CMB}}(\hat{n}) \delta^2 Q_{\text{CIB}}(\hat{n}) \rangle \Big] \\
+& \delta^2 E_{\text{CMB}}(\hat{n}) \langle P_{\text{CMB}}(\hat{n}) Q_{\text{CIB}}(\hat{n}) \rangle - \delta^2 P_{\text{CMB}}(\hat{n}) \langle E_{\text{CMB}}(\hat{n}) Q_{\text{CIB}}(\hat{n}) \rangle \\
+& P_{\text{CMB}}(\hat{n}) \Big[\langle Q_{\text{CIB}}(\hat{n}) \delta^2 E_{\text{CMB}}(\hat{n}) \rangle - \langle E_{\text{CMB}}(\hat{n}) \delta^2 Q_{\text{CIB}}(\hat{n}) \rangle \Big] \Big\}. \tag{65}
\end{aligned}
$$

6 SUMMARY AND CONCLUSIONS

In this paper we have investigated the NG signal arising from the CIB and its correlation with the lensing signal imprinted in the CMB temperature anisotropies, and we have estimated the bias they can induce on the local, equilateral and orthogonal f_{nl} parameter using *Planck* data. The bias is computed for 'raw' single–frequency temperature maps, i.e. maps on which no component separation is applied, and for maps cleaned by the SEVEM component separation technique. For these maps, we have used the *Planck* instrumental characteristics and we have assumed they are free from Galactic foregrounds. We have then studied the possibility to detect the CIB–lensing bispectrum in the *Planck* data.

CIB intensity fluctuations have been modelled following Planck early results XVIII (2011). The parameters of the model have been updated in order to have a better agreement with the recent *Planck* measurements of the CIB power spectra (Planck 2013 results XXX 2014). We have also considered the contribution from extragalactic radio sources and from their correlation with CMB lensing. As expected, radio–lensing power spectra and bispectra are found to be small and negligible at the frequencies used for the cosmological analysis in *Planck*.

Below we summarise and discuss our results.

- The bias Δf_{nl} induced by the CIB–lensing correlation is small but not negligible for orthogonal shapes in the "raw" 143 and 217 GHz *Planck* maps, approximately -21 and -88 respectively. However, when maps are cleaned with a component separation technique, the bias is strongly reduced and becomes almost negligible for *Planck* results (the largest bias appears for the orthogonal shape and amounts to $0.3\,\sigma$).
- We have estimated the bias produced by the intrinsic bispectrum of extragalactic sources. In agreement with the discussion in Planck 2013 results XXIV (2014), point sources turn out to be not a severe contaminant for f_{nl} studies with *Planck* foreground–reduced data, even though not completely negligible (the largest bias is for the equilateral shape amounting to $0.45\,\sigma$). In "raw" maps they produce a significant bias only for equilateral shapes, that is 160, 54 and 60 at 100, 143 and 217 GHz respectively.
- Our results confirm the capability and stress the importance of component separation techniques in removing extragalactic foregrounds as well. On the other hand, our results also predict that future experiments, with better sensitivity to the f_{nl} parameter, might have to consider extragalactic sources and the CIB–lensing correlation as further serious contaminants in some particular shapes.

• The detection of the CIB–lensing bispectrum signal directly from *Planck* maps is not straightforward and it is feasible only for the 217 GHz channel (with a significance of $\sim 7.5\,\sigma$, assuming full sky coverage). Nevertheless, we have shown in this paper that a more efficient way to detect the bispectrum cross–correlates CMB maps with CIB maps at different frequencies. In this case the CIB–lensing bispectrum signal could be detected with very high significance ($\lesssim 63\,\sigma$) if accurate CIB maps can be extracted at 353, 545 and 857 GHz over a large area of the sky. Planck 2013 results XXX (2014) were able to produce clean CIB maps just over $\approx 10\%$ of the sky; in this case we still expect a high level of significance, of approximately $20\,\sigma$ or more. We have to note however that the cross correlation between CMB and CIB maps is not a simple procedure as possible residuals of the CIB (CMB) in "clean" CMB (CIB) maps could produce spurious signals that can be easily misinterpreted.

• We have compared our predictions for the detectability levels of the CIB–lensing bispectrum on *Planck* data with the results already obtained by the *Planck* Collaboration using the cross-spectrum estimator (Planck 2013 results XVIII 2014). Our results are nearly equivalent to the ones presented in that work when we compare the case with $f_{sky} = 30.4\%$, the lensing reconstruction at 143 GHz and the CIB dominated bands of 353, 545 and 857 GHz (see Table 7). This shows that both approaches are equivalent in terms of efficiency and both of them can be used to provide more robust results as different estimators might have different sensitivity to systematics.

• Finally, we have developed an optimal estimator for the CIB–lensing bispectrum, based on the KSW formalism. Two different estimators have been constructed, one for use with single–frequency maps and a second one for separate CMB and CIB maps.

REFERENCES

Argüeso F., González-Nuevo J., Toffolatti L., 2003, ApJ, 598, 86
Bartolo N., Komatsu E., Matarrese S., Riotto A., 2004, Phys. Rep., 402, 103
Bartolo N., Matarrese S., Riotto A., 2010, Adv. Astron., 2010
Béthermin M., Dole H., Lagache G., Le Borgne D., Penin A., 2011, A&A, 529, A4
Boughn S. P., Crittenden R. G., 2005, New Astron. Rev., 49, 75
Chatterjee S., Degraf C., Richardson J., Zheng Z., Nagai D., Di Matteo T., 2012, MNRAS, 419, 2657
Condon J. J., Cotton W. D., Greisen E. W., Yin Q. F., Perley R. A., Taylor G. B., Broderick J. J., 1998, AJ, 115, 1693
Cooray A., Hu W., 2000, ApJ, 534, 533
Cooray A., Sheth R., 2002, Phys. Rep., 372, 1
Curto A., Tucci M., González-Nuevo J., Toffolatti L., Martínez-González E., Argüeso F., Lapi A., López-Caniego M., 2013, MNRAS, 432, 728
Fernández-Cobos R., Vielva P., Barreiro R. B., Martínez-González E., 2012, MNRAS, 420, 2162
Goldberg D. M., Spergel D. N., 1999, Phys.Rev., D59, 103002
González-Nuevo J., Toffolatti L., Argüeso F., 2005, ApJ, 621, 1
Górski K. M., Hivon E., Banday A. J., Wandelt B. D., Hansen F. K., Reinecke M., Bartelmann M., 2005, ApJ, 622, 759
Hu W., 2000, Phys. Rev. D, 62, 043007
Komatsu E., Spergel D. N., 2001, Phys. Rev. D, 63, 063002
Komatsu E., Spergel D. N., Wandelt B. D., 2005, ApJ, 634, 14
Kravtsov A. V., Berlind A. A., Wechsler R. H., Klypin A. A., Gottlöber S., Allgood B., Primack, J. R., 2004, ApJ, 609, 35
Lacasa F., Aghanim N., 2012, preprint (arXiv:1211.3902)
Lacasa F., Aghanim N., Kunz M., Frommert M., 2012, MNRAS, 421, 1982
Lacasa F., Pénin A., Aghanim N., 2014, MNRAS, 439, 123
Lagache G., Dole H., Puget J.-L., Pérez-González P. G., Le Floc'h E., Rieke G. H., Papovich C., Egami E., Alonso-Herrero A., Engelbracht C. W., Gordon K. D., Misselt K. A., Morrison J. E., 2004, ApJS, 154, 112
Leach S. M., Cardoso J.-F., Baccigalupi C., Barreiro R. B., Betoule M., Bobin J., Bonaldi A., et al. 2008, A&A, 491, 597
Lewis A., Challinor A., Lasenby A., 2000, ApJ, 538, 473
Lewis A., Challinor A., 2006, Phys. Rep., 429, 1
Lewis A., Challinor A., Hanson D., 2011, J. Cosmol. Astropart. Phys., 3, 18

Liguori M., Sefusatti E., Fergusson J. R., Shellard E. P. S., 2010, Adv. Astron., 2010

Mangilli A., Wandelt B., Elsner F., Liguori M., 2013, A&A, 555, A82

Marcos-Caballero A., Vielva P., Martinez-Gonzalez E., Finelli F., Gruppuso A., Schiavon F., 2013, preprint (arXiv:1312.0530)

Martínez-González E. & Planck Collaboration 2012, AIP Conf. Ser. Vol. 1458, 'The Planck mission and the cosmological paradigm'. pp 190–206

Navarro J. F., Frenk C. S., White S. D. M., 1997, ApJ, 490, 493

Negrello M., Perrotta F., González-Nuevo J., Silva L., de Zotti G., Granato G. L., Baccigalupi C., Danese L., 2007, MNRAS, 377, 1557

Pénin A., Doré O., Lagache G., Béthermin M., 2012, A&A, 537, A137

Pénin A., Lacasa F., Aghanim N., 2014, MNRAS, 439, 143

Planck Collaboration, 2011, A&A, 536, A18

Planck Collaboration, 2014, A&A, 571, A1

Planck Collaboration, 2014, A&A, 571, A12

Planck Collaboration, 2014, A&A, 571, A16

Planck Collaboration, 2014, A&A, 571, A17

Planck Collaboration, 2014, A&A, 571, A18

Planck Collaboration, 2014, A&A, 571, A19

Planck Collaboration, 2014, A&A, 571, A23

Planck Collaboration, 2014, A&A, 571, A24

Planck Collaboration, 2014, A&A, 571, A28

Planck Collaboration, 2014, A&A, 571, A30

Planck Collaboration, 2015, preprint (arXiv:1502.01594)

Scherrer R.J., Bertschinger E., 1991, ApJ, 381, 349

Scoccimarro R., Sheth R. K., Hui L., Jain B., 2001, ApJ, 546, 20

Seljak U., 2000, MNRAS, 318, 203

Song Y.-S., Cooray A., Knox L., Zaldarriaga M., 2003, ApJ, 590, 664

Tinker J., Kravtsov A. V., Klypin A., Abazajian K., Warren M., Yepes G., Gottlöber S., Holz D. E., 2008, ApJ, 688, 709

Tinker J. L., Wetzel A. R., 2010, ApJ, 719, 88

Tinker J. L., Wechsler R. H., Zheng Z., 2010, ApJ, 709, 67

Toffolatti L., Negrello M., González-Nuevo J., de Zotti G., Silva L., Granato G. L., Argüeso F., 2005, A&A, 438, 475

Tucci M., Toffolatti L., de Zotti G., Martínez-González E., 2011, A&A, 533, A57

Vielva P., Martínez-González E., Tucci M., 2006, MNRAS, 365, 891

Yadav A. P. S., Wandelt B. D., 2010, Adv. Astron., 2010, 565248

Zheng Z., Berlind A.A., Weinberg D.H., Benson A.J., Baugh C.M., Cole S., Davé R., et al., 2005, ApJ, 633, 791

APPENDIX A: CIB–LENSING POWER SPECTRUM AT LARGE SCALES

In this Appendix we derive the angular power spectrum for the CIB–lensing correlation given in Eqs. (7) and (13). Starting from the angular correlation function of CIB fluctuations and lensing potential, the procedure is equivalent to the one presented in Lewis & Challinor (2006) for the lensing power spectrum (see also, e.g., Cooray & Hu 2000).

We write fluctuations of the CIB temperature in a direction $\hat{\mathbf{n}}$ at frequency ν as

$$T_\nu^{(\text{CIB})}(\hat{\mathbf{n}}) = \int d\chi \, a(\chi) \bar{j}_\nu(\chi) \frac{\delta j_\nu(\chi \hat{\mathbf{n}}, \chi)}{\bar{j}_\nu(\chi)} = \int d\chi \, W_\nu^{(\text{CIB})}(\chi) \delta_{\text{gal}}(\chi \hat{\mathbf{n}}, \chi, \nu) \,, \tag{A1}$$

where χ is the comoving distance, $j_\nu(\chi)$ is the CIB emissivity and $a(\chi)$ is the scale factor. Here we have assumed that fluctuations in CIB emissivity, $\delta j_\nu(z)/\bar{j}_\nu(z)$, trace fluctuations in the number density of galaxies, $\delta_{\text{gal}}(z, \nu)$, with $n_{\text{gal}} = \bar{n}_{\text{gal}}(1 + \delta_{\text{gal}})$. On the other hand, the lensing potential along the line of sight is usually defined in terms of the gravitational potential Φ by

$$\phi(\hat{\mathbf{n}}) = -2 \int_0^{\chi_*} d\chi \, \frac{\chi_* - \chi}{\chi \chi_*} \Phi(\chi \hat{\mathbf{n}}, \chi) \,. \tag{A2}$$

The gravitational potential field is related to the matter density field δ_{m}[8] by the Poisson equation and the lensing potential can be written as

$$\phi(\hat{\mathbf{n}}) = \int_0^{\chi_*} d\chi \int \frac{d^3\mathbf{k}}{(2\pi)^{3/2}} W^{(\text{Lens})}(k, \chi) \delta_{\text{m}}(k, \chi) e^{i\chi \mathbf{k} \cdot \hat{\mathbf{n}}} \,, \tag{A3}$$

where $\delta_{\text{m}}(k, \chi)$ is the Fourier transform of the matter density field. The functions $W^{(\text{CIB})}$ and $W^{(\text{Lens})}$ are the same as in Eq. (8).

---

[8] Here we assume that the anisotropic stress in the Universe is negligible so that the two Bardeen potentials Φ and Ψ coincide. In general one needs to consider the Weyl potential $(\Phi + \Psi)/2$ which governs the lensing of light. However, the approximations made here are very good in a ΛCDM universe and for the redshift range considered.

After introducing the Fourier transforms of CIB and matter fluctuations, the cross–correlation between the lensing potential and the CIB fluctuations is

$$\langle T_\nu^{(\mathrm{CIB})}(\hat{\mathbf{n}})\phi(\hat{\mathbf{n}}')\rangle = \int_0^{\chi_*} d\chi\, W_\nu^{(\mathrm{CIB})}(\chi) \int_0^{\chi_*} d\chi' \int \frac{d^3\mathbf{k}d^3\mathbf{k}'}{(2\pi)^3} W^{(\mathrm{Lens})}(k',\chi')\langle\delta_{\mathrm{gal}}(k,\chi,\nu)\delta_m^*(k',\chi')\rangle e^{i\chi\mathbf{k}\cdot\hat{\mathbf{n}}}e^{-i\chi\mathbf{k}'\cdot\hat{\mathbf{n}}'}, \quad (A4)$$

where

$$\langle\delta_{\mathrm{gal}}(k,\chi,\nu)\delta_m^*(k',\chi')\rangle = P_{\delta g}(k,\chi,\chi',\nu)\delta(\mathbf{k}-\mathbf{k}') \quad (A5)$$

and $P_{\delta g}(k)$ is the power spectrum of the cross–correlation between galaxy number density and matter fluctuations.

Using the relation

$$e^{i\chi\mathbf{k}\cdot\hat{\mathbf{n}}} = 4\pi\sum_{\ell m} i^\ell j_\ell(k\chi)Y_{\ell m}^*(\hat{\mathbf{n}})Y_{\ell m}(\hat{\mathbf{k}}), \quad (A6)$$

and the orthogonality of the spherical harmonics we have

$$\langle T_\nu^{(\mathrm{CIB})}(\hat{\mathbf{n}})\phi(\hat{\mathbf{n}}')\rangle = \frac{2}{\pi}\sum_{\ell\ell' mm'}\int_0^{\chi_*} d\chi\, W_\nu^{(\mathrm{CIB})}(\chi) \int_0^{\chi_*} d\chi' \times$$
$$\times \int dk\, k^2 W^{(\mathrm{Lens})}(k,\chi')P_{\delta g}(k,\chi,\chi',\nu)j_\ell(k\chi)j_{\ell'}(k\chi')Y_{\ell m}(\hat{\mathbf{n}})Y_{\ell' m'}^*(\hat{\mathbf{n}}')\delta_{\ell\ell'}\delta_{mm'}. \quad (A7)$$

From the last equation it is straightforward to get the power spectrum of the CIB–lensing correlation

$$C_\ell^{(\mathrm{CIB-Lens})}(\nu) = \frac{2}{\pi}\int dk\, k^2 \int_0^{\chi_*} d\chi\, W_\nu^{(\mathrm{CIB})}(\chi)j_\ell(k\chi) \int_0^{\chi_*} d\chi'\, W^{(\mathrm{Lens})}(k,\chi')j_\ell(k\chi')P_{\delta g}(k,\chi,\chi',\nu). \quad (A8)$$

In the HOD approach, at very large scales $P_{\delta g}(k)$ is dominated by the 2–halo term (at $\ell = 40$ the 1–halo term in fact contributes just for $\sim 1\%$). Under this condition, both matter and CIB fluctuations can be related to linear density perturbations $\delta_{\mathrm{lin}}(\mathbf{k})$ through a transfer function $\mathcal{T}_X(k,\chi)$ so that $\delta_X(\mathbf{k},\chi) = \mathcal{T}_X(k,\chi)\delta_{\mathrm{lin}}(\mathbf{k})$, with $X = \mathrm{gal, m}$. Therefore $C_\ell^{(\mathrm{CIB-Lens})}$ becomes

$$C_\ell^{(\mathrm{CIB-Lens})}(\nu) = \frac{2}{\pi}\int dk\, k^2 P_{\mathrm{lin}}(k) \int_0^{\chi_*} d\chi\, W_\nu^{(\mathrm{CIB})}(\chi)\mathcal{T}_{\mathrm{gal}}(k,\chi,\nu)j_\ell(k\chi) \int_0^{\chi_*} d\chi'\, W^{(\mathrm{Lens})}(k,\chi')\mathcal{T}_{\mathrm{m}}(k,\chi')j_\ell(k\chi') \quad (A9)$$

Because the power spectrum of galaxies, $P_{\mathrm{gg}}(k)$, and of dark matter perturbations, $P_{\delta\delta}(k)$, are

$$P_{\mathrm{gg}}(k,\chi,\nu) = \langle\delta_{\mathrm{gal}}(k,\chi,\nu)\delta_{\mathrm{gal}}^*(k,\chi,\nu)\rangle = P_{\mathrm{lin}}(k)\mathcal{T}_{\mathrm{gal}}^2(k,\chi,\nu); \quad P_{\delta\delta}(k,\chi) = \langle\delta_{\mathrm{m}}(k,\chi)\delta_{\mathrm{m}}^*(k,\chi)\rangle = P_{\mathrm{lin}}(k)\mathcal{T}_{\mathrm{m}}^2(k,\chi), \quad (A10)$$

we find

$$C_\ell^{(\mathrm{CIB-Lens})}(\nu) = \frac{2}{\pi}\int dk\, k^2 \int_0^{\chi_*} d\chi\, W_\nu^{(\mathrm{CIB})}(\chi)j_\ell(k\chi)\sqrt{P_{gg}(k,\chi,\nu)} \int_0^{\chi_*} d\chi'\, W^{(\mathrm{Lens})}(k,\chi')j_\ell(k\chi')\sqrt{P_{\delta\delta}(k,\chi')}, \quad (A11)$$

as in Eq. (13).

At high ℓ, the cross–correlation power spectrum $P_{\delta g}(k,\chi,\chi',)$ in Eq. (A8) is expected to vary slowly compared to spherical Bessel functions, and we can perform the k-integration taking the power spectrum constant. The spherical Bessel functions then give a delta-function,

$$\int dk\, k^2 j_\ell(k\chi)j_\ell(k\chi') = \frac{2}{\pi\chi^2}\delta(\chi-\chi'), \quad (A12)$$

which allows us to perform one of the χ integrations as well and which fixes the scale $k \sim \ell/\chi$. We then obtain $C_\ell^{\mathrm{CIB-Lens}}$ in the Limber approximation

$$C_\ell^{(\mathrm{CIB-Lens})}(\nu) = \int_0^{\chi_*} \frac{d\chi}{\chi^2} W_\nu^{(\mathrm{CIB})}(\chi)W^{(\mathrm{Lens})}(k,\chi)P_{\delta g}(k=\ell/\chi,\chi,\nu). \quad (A13)$$

APPENDIX B: HOD MODEL CONSTRAINTS FROM *Planck* DATA

In this appendix we find the best–fit values for the HOD parameters used in Section 2 to model CIB and CIB–lensing spectra. The free parameters are simply M_{min} and α_{sat}, after imposing $M_{\mathrm{sat}} = 3.3 M_{\mathrm{min}}$ and $\sigma_{\log M} = 0.65$. Another free parameter is the effective mean emissivity j_{eff}. In order to isolate and constrain the high–z contribution to the CIB that is poorly known from observations, we make in fact the extra assumption that the mean emissivity of galaxies, j_{eff}, is constant at $z > 3.5$ (Planck early results XVIII 2011). More precisely, Eq. (7) is rewritten as

$$C_\ell^{(\mathrm{CIB})}(\nu,\nu') = \int_0^{3.5} \frac{d\chi}{\chi^2} a^2(\chi)\bar{j}_\nu(\chi)\bar{j}_{\nu'}(\chi)P_{\mathrm{gg}}(k=\ell/\chi,\chi) + j_{\mathrm{eff}}(\nu)j_{\mathrm{eff}}(\nu')\int_{3.5}^7 \frac{d\chi}{\chi^2} a^2(\chi)P_{\mathrm{gg}}(k=\ell/\chi,\chi). \quad (B1)$$

The three parameters of the model are fitted to the CIB spectra measured in Planck 2013 results XXX (2014), using a Markov Chain Monte Carlo (MCMC) method. For each *Planck* frequency $\geqslant 217$ GHz we find the values of M_{min}, α_{sat} and j_{eff} that best fit the CIB power spectrum $C_\ell^{(\mathrm{CIB})}(\nu)$ at the corresponding frequency, and their associated uncertainties. For the 143 GHz channel we prefer to use the 143×857 and 143×545 cross–power spectra, due to the large uncertainty in the 143×143 spectrum. Finally, at 100 GHz we take the same HOD values as

Table B1. Best–fit values for the parameters of the CIB model, and the corresponding reduced chi–squared, $\chi^2_{\rm red}$.

Frequency	[GHz]	143	217	353	545	857
$\log M_{\rm min}$	$[M_\odot]$	11.33 ± 0.56	11.90 ± 0.52	12.45 ± 0.33	12.10 ± 0.14	11.62 ± 0.27
$\alpha_{\rm sat}$		0.65 ± 0.22	1.37 ± 0.26	1.21 ± 0.20	1.01 ± 0.04	0.86 ± 0.06
$j_{\rm eff}$	[Jy/Mpc/sr]	15.3 ± 5.4	$61. \pm 13.$	$191. \pm 33.$	$538. \pm 38.$	$1326. \pm 160.$
$\chi^2_{\rm red}$		0.73	0.45	0.73	3.03	1.16

at 143 GHz and $j_{\rm eff} = 4.15$ Jy/Mpc/sr, that corresponds to the average emissivity between $z = 3.5$ and 7 according to the Béthermin et al. (2011) model.

Because it is not possible to disentangle the shot–noise contributions of radio and IR galaxies from observations, we fix them on the basis of the Tucci et al. (2011) and Béthermin et al. (2011) models.

In Table B1 we report our results for the free parameters with the corresponding reduced chi–squared $\chi^2_{\rm red}$ of the fits (for 8 degrees of freedom except at 143 GHz where we have 16). Comparing to the parameter values found in Planck early results XVIII (2011), we obtain very similar results for the 217 and 353 GHz channels. At 545 and 857 GHz our best–fit values for $M_{\rm min}$ and $\alpha_{\rm sat}$ are slightly different from *Planck* results, but still compatible at 1–σ. The only (small) discrepancy is on $j_{\rm eff}$: the *Planck* best–fits are around 300 Jy/Mpc/sr at the two frequencies and compatible with zero. Planck 2013 results XVIII (2014, see their Table 3) also estimated the mean CIB emissivity in the redshift bin $3 < z \leqslant 7$ and found 417 ± 251 Jy/Mpc/sr at 545 GHz and 609 ± 359 Jy/Mpc/sr at 857 GHz. According to our results, high–redshift galaxies seem to give a bigger contribution at these frequencies, especially at 857 GHz.

In Figure B1 we compare the model predictions with *Planck* observations. The fit of the model is in general good at the high frequencies, both for auto– and cross–spectra (it is to be stressed that cross-spectra, $C_\ell^{\rm (CIB)}(\nu, \nu')$, have not been used in the fitting procedure). The reduced chi–squared for the 857×545 and 545×545 spectra is quite large. However, due to the very small uncertainty on data, even for these cases the model can be considered a reasonable description of the data. Some discrepancies are found for all the cross–spectra involving the 217 GHz data and for the 143×143 and 143×217 spectra. The latter spectra are however particularly problematic due to the subtraction of CMB anisotropies and to spurious CIB and SZ signals that have to be corrected (Planck 2013 results XXX 2014). Finally, Figure B2 shows the CIB–lensing spectra from the model and from the data: the agreement is generally quite good for all the *Planck* channels.

APPENDIX C: SHOT–NOISE CROSS–POWER SPECTRA AND BISPECTRA FROM EXTRAGALACTIC SOURCES

The shot–noise power spectrum and bispectrum from extragalactic sources at a fixed frequency ν can be computed by the well known integrals:

$$C_{\rm sn} = \int_0^{S_c} \frac{dN}{dS} S^2 dS \qquad b_{\rm sn} = \int_0^{S_c} \frac{dN}{dS} S^3 dS \,, \tag{C1}$$

where S_c is the flux cut above which bright sources are detected and removed, and dN/dS are differential number counts of sources. When different frequencies are considered, we use two different approaches for computing the cross–power spectra and bispectra, according to the class of extragalactic sources.

- For IR galaxies we use the same approach as in Planck 2013 results XXX (2014): the cross–spectra and bispectra for a single galaxy population can be approximated by

$$
\begin{aligned}
C_{\rm sn}(\nu_1, \nu_2) &= \int_{z=0}^{7} \int_0^{S_c(\nu_1)} H(S_{\nu_1} R_{\nu_1 \nu_2} < S_c(\nu_2)) \frac{dN}{dS_{\nu_1} dz} S_{\nu_1}^2 R_{\nu_1 \nu_2}(S_{\nu_1}, z) \, dS_{\nu_1} dz \\
b_{\rm sn}(\nu_1, \nu_2, \nu_3) &= \int_{z=0}^{7} \int_0^{S_c(\nu_1)} H(S_{\nu_1} R_{\nu_1 \nu_2} < S_c(\nu_2)) H(S_{\nu_1} R_{\nu_1 \nu_3} < S_c(\nu_3)) \times \\
&\quad \times \frac{dN}{dS_{\nu_1} dz} S_{\nu_1}^3 R_{\nu_1 \nu_2}(S_{\nu_1}, z) R_{\nu_1 \nu_3}(S_{\nu_1}, z) \, dS_{\nu_1} dz \,,
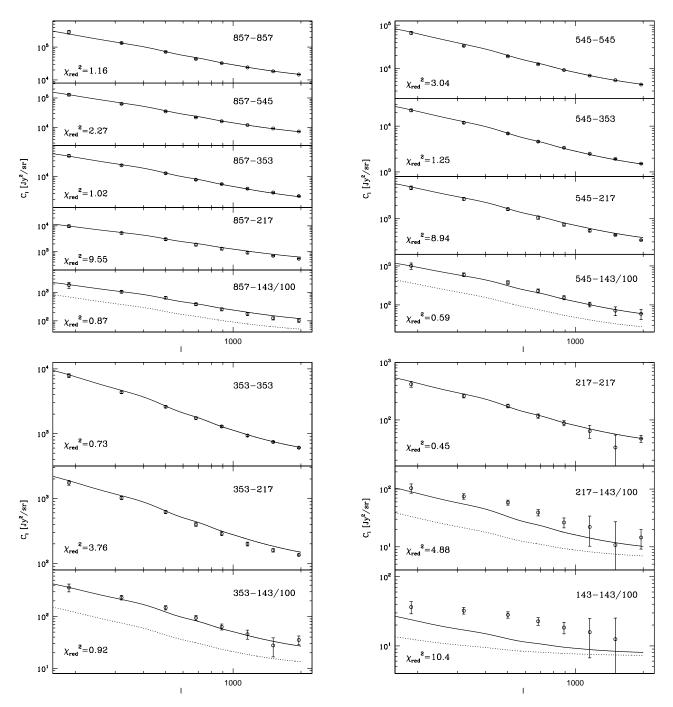\end{aligned}
\tag{C2}
$$

where $R_{\nu_1 \nu_2}(S_{\nu_1}, z)$ is the mean colour between ν_1 and ν_2 in the considered flux density and redshift interval (i.e., the flux density at ν_2 is written as $S_{\nu_2} = R_{\nu_1 \nu_2} S_{\nu_1}$). We compute the mean colour from the Béthermin et al. (2011) model. $H(P_1)$ is equal to 1 when P_1 is true and 0 otherwise.

- The approach used for IR galaxies cannot be safely applied to radio sources because of the very large dispersion in the spectral shape of radio sources. When two different frequencies ν_1 and ν_2 are considered, we compute the cross–power spectra and bispectra of radio sources as a direct extension of Eq. (C1):

$$
\begin{aligned}
C_{\rm sn}(\nu_1, \nu_2) &= \int_0^{S_c(\nu_1)} dS_{\nu_1} \, S_{\nu_1} \int_0^{S_c(\nu_2)} dS_{\nu_2} \, \frac{d^2 N}{dS_{\nu_1} dS_{\nu_2}} S_{\nu_2} \\
b_{\rm sn}(\nu_1, \nu_1, \nu_2) &= \int_0^{S_c(\nu_1)} dS_{\nu_1} \, S_{\nu_1}^2 \int_0^{S_c(\nu_2)} dS_{\nu_2} \, \frac{d^2 N}{dS_{\nu_1} dS_{\nu_2}} S_{\nu_2} \,,
\end{aligned}
\tag{C3}
$$

Figure B1. Auto– and cross–power spectra of CIB fluctuations measured by *Planck* at the HFI frequencies (Planck 2013 results XXX 2014, open points), compared with predictions of our best–fit model (solid lines). Dotted lines are for spectra involving the 100 GHz channel. Data and predictions include also contributions from radio and IR shot noise. The reduced χ^2 of the fits are also provided.

where $d^2N/dS_{\nu_1}dS_{\nu_2}$ is the differential number of sources with flux density in the interval $[S_{\nu_1}, S_{\nu_1} + \Delta S]$ at the frequency ν_1 and with flux density in the interval $[S_{\nu_2}, S_{\nu_2} + \Delta S]$ at the frequency ν_2. The shot noise bispectra at the frequencies ν_1, ν_2 and ν_3 require to compute differential number counts ($d^3N/dS_{\nu_1}dS_{\nu_2}dS_{\nu_3}$) at the three different flux density intervals, one for each frequency. This is too complex and time consuming to be carried out in practice. For this reason we decided to approximate the "cross" bispectra in the following way. For a single population of radio sources, in the hypothesis of a full correlation between two frequencies ν_2 and ν_3 (i.e., $S_{\nu_3} = S_{\nu_2}R_{\nu_2\nu_3}$), we
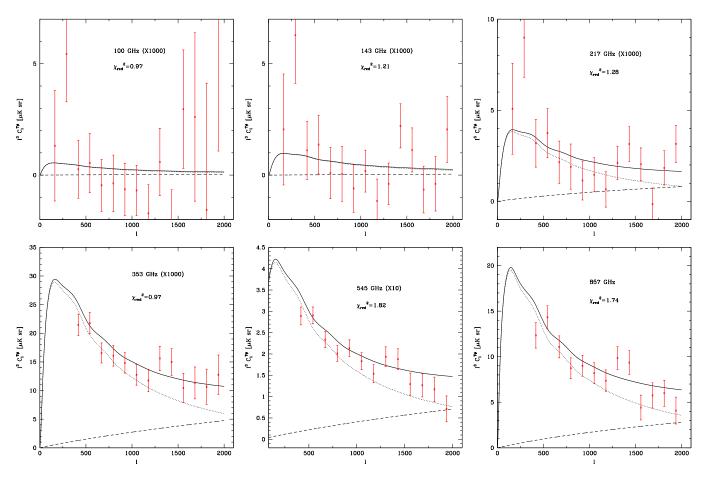
Figure B2. CIB–Lensing power spectra from Planck 2013 results XXX (2014), compared with predictions of our best–fit model: solid lines are for total spectra; dotted(dashed) lines are for the 2–(1–)halo term. The reduced χ^2 of the fits are also provided.

have

$$
\begin{aligned}
b_{\rm sn}(\nu_1, \nu_2, \nu_3) &= \int_0^{S_c(\nu_1)} dS_{\nu_1} \, S_{\nu_1} \int_0^{S_c(\nu_2)} dS_{\nu_2} \, S_{\nu_2} \int_0^{S_c(\nu_3)} dS_{\nu_3} \, S_{\nu_3} \frac{d^3 N}{dS_{\nu_1} dS_{\nu_2} dS_{\nu_3}} \\
&= \int_0^{S_c(\nu_1)} dS_{\nu_1} \, S_{\nu_1} \int_0^{S_c(\nu_2)} dS_{\nu_2} \, S_{\nu_2}^2 \frac{d^2 N}{dS_{\nu_1} dS_{\nu_2}} R_{\nu_2 \nu_3} H(S_{\nu_2} R_{\nu_2 \nu_3} < S_c(\nu_3)) = b_{\rm sn}(\nu_1, \nu_2, \nu_2) R_{\nu_2 \nu_3}
\end{aligned}
\tag{C4}
$$

where the mean colour $R_{\nu_2 \nu_3}$ has been assumed independent of the flux density, and $S_c(\nu_2) R_{\nu_2 \nu_3} < S_c(\nu_3)$. A better approximation for the "cross" bispectra can be obtained by replacing $R_{\nu_2 \nu_3}$ with the "decorrelation" coefficient, $C_{\rm sn}(\nu_2, \nu_3)/[C_{\rm sn}(\nu_2, \nu_2) C_{\rm sn}(\nu_3, \nu_3)]^{1/2}$, that provides a measure of the frequency correlation of radio sources. Considering all the possible combinations in frequency, we get

$$
b_{\rm sn}(\nu_1, \nu_2, \nu_3) \approx \left[\prod_{\substack{i=1,3 \\ j=1,3;\, j \neq i}} \tilde{b}_{\rm sn}(\nu_i, \nu_i, \nu_j) \right]^{1/6} \quad \text{with} \quad \tilde{b}_{\rm sn}(\nu_i, \nu_i, \nu_j) = b_{\rm sn}(\nu_i, \nu_i, \nu_j) \frac{C_{\rm sn}(\nu_i, \nu_k)}{[C_{\rm sn}(\nu_i, \nu_i) C_{\rm sn}(\nu_k, \nu_k)]^{1/2}} \quad \text{and } k \neq i, j \, .
\tag{C5}
$$

This expression is an upper limit of the actual bispectrum, but we expect it to be a good approximation for frequencies where the correlation is high. We applied Eq. (C5) to the CIB and we found values typically 20–30% higher than ones from Eq. (C2), but very close when adjacent frequencies are considered. We have also verified that the bias on the $f_{\rm nl}$ parameter does not change if we take $\tilde{b}_{\rm sn}(\nu_i, \nu_i, \nu_j) = b_{\rm sn}(\nu_i, \nu_i, \nu_j)$ in Eq. (C5). This confirms the very small impact of the cross bispectra of radio sources on the $f_{\rm nl}$ bias in the SEVEM combined maps.

APPENDIX D: COVARIANCE OF THE CIB-LENSING BISPECTRUM

We estimate the covariance matrix of the CIB–lensing bispectrum taking into account higher order corrections for the cases where the non-Gaussian signal becomes significant. The covariance of the CIB–lensing bispectrum is given by

$$
{\rm cov}\left(b_{\ell_1 \ell_2 \ell_3}^{({\rm CIB-Lens})}, b_{\ell_1' \ell_2' \ell_3'}^{({\rm CIB-Lens})} \right) = \langle b_{\ell_1 \ell_2 \ell_3}^{({\rm CIB-Lens})} b_{\ell_1' \ell_2' \ell_3'}^{({\rm CIB-Lens})} \rangle - \langle b_{\ell_1 \ell_2 \ell_3}^{({\rm CIB-Lens})} \rangle \langle b_{\ell_1' \ell_2' \ell_3'}^{({\rm CIB-Lens})} \rangle,
\tag{D1}
$$

where

$$b_{\ell_1\ell_2\ell_3}^{\text{(CIB-Lens)}} \equiv \frac{1}{I_{\ell_1\ell_2\ell_3}} \sum_{m_1m_2m_3} \begin{pmatrix} \ell_1 & \ell_2 & \ell_3 \\ m_1 & m_2 & m_3 \end{pmatrix} \left(B^{\text{(CIB-Lens)}}\right)_{\ell_1\ell_2\ell_3}^{m_1m_2m_3} = \frac{1}{I_{\ell_1\ell_2\ell_3}} \sum_{m_1m_2m_3} \begin{pmatrix} \ell_1 & \ell_2 & \ell_3 \\ m_1 & m_2 & m_3 \end{pmatrix} \tilde{a}_{\ell_1m_1}^{\text{(CMB)}} \tilde{a}_{\ell_2m_2}^{\text{(CMB)}} a_{\ell_3m_3}^{\text{(CIB)}}, \quad \text{(D2)}$$

$a_{\ell m}^{\text{(CIB)}}$ are the spherical harmonic coefficients of the CIB map, $\tilde{a}_{\ell m}^{\text{(CIB)}}$ are the spherical harmonic coefficients of the CMB map, including the effect of the lensing up to first order on the primordial $a_{\ell m}^{\text{(CMB)}}$:

$$\tilde{a}_{\ell m}^{\text{(CMB)}} = a_{\ell m}^{\text{(CMB)}} + \sum_{\ell'm'\ell''m''} (-1)^m G_{\ell\ell'\ell''}^{mm'm''} \left[\frac{\ell'(\ell'+1) - \ell(\ell+1) + \ell''(\ell''+1)}{2} a_{\ell'm'}^{\text{(CMB)}} \phi_{\ell''m''}\right] \equiv a_{\ell m}^{\text{(CMB)}} + (a\phi)_{\ell m}. \quad \text{(D3)}$$

The expected average of the CIB–lensing bispectrum is

$$\langle b_{\ell_1\ell_2\ell_3}^{\text{(CIB-Lens)}} \rangle = b_{\ell_1\ell_2\ell_3}^{\text{(CIB-Lens)}} = \frac{\ell_1(\ell_1+1) - \ell_2(\ell_2+1) + \ell_3(\ell_3+1)}{2} C_{\ell_3}^{\text{(CIB-Lens},\nu)} \tilde{C}_{\ell_1}^{\text{(CMB)}}$$
$$+ \frac{\ell_2(\ell_2+1) - \ell_1(\ell_1+1) + \ell_3(\ell_3+1)}{2} C_{\ell_3}^{\text{(CIB-Lens},\nu)} \tilde{C}_{\ell_2}^{\text{(CMB)}}. \quad \text{(D4)}$$

The correlation term in Eq. (D1) is given by:

$$\langle b_{\ell_1\ell_2\ell_3}^{\text{(CIB-Lens)}} b_{\ell_1'\ell_2'\ell_3'}^{\text{(CIB-Lens)}} \rangle = \frac{1}{I_{\ell_1\ell_2\ell_3} I_{\ell_1'\ell_2'\ell_3'}} \sum_{m_1m_2m_3} \sum_{m_1'm_2'm_3'} \begin{pmatrix} \ell_1 & \ell_2 & \ell_3 \\ m_1 & m_2 & m_3 \end{pmatrix} \begin{pmatrix} \ell_1' & \ell_2' & \ell_3' \\ m_1' & m_2' & m_3' \end{pmatrix} \langle \tilde{a}_{\ell_1m_1}^{\text{(CMB)}} \tilde{a}_{\ell_2m_2}^{\text{(CMB)}} a_{\ell_3m_3}^{\text{(CIB)}} \tilde{a}_{\ell_1'm_1'}^{\text{(CMB)}} \tilde{a}_{\ell_2'm_2'}^{\text{(CMB)}} a_{\ell_3'm_3'}^{\text{(CIB)}} \rangle. \quad \text{(D5)}$$

Considering 6 random variables, x_1, x_2, x_3, x_4, x_5, x_6 with significant departures from Gaussianity due to their bispectrum, and neglecting the trispectrum and higher order terms, their sixth order moment is expanded as:

$$\langle x_1x_2x_3x_4x_5x_6 \rangle = \langle x_1x_2 \rangle\langle x_3x_4 \rangle\langle x_5x_6 \rangle + \langle x_1x_2 \rangle\langle x_3x_5 \rangle\langle x_4x_6 \rangle + \langle x_1x_2 \rangle\langle x_3x_6 \rangle\langle x_4x_5 \rangle + \langle x_1x_3 \rangle\langle x_2x_5 \rangle\langle x_4x_6 \rangle$$
$$+ \langle x_1x_3 \rangle\langle x_2x_6 \rangle\langle x_4x_5 \rangle + \langle x_1x_3 \rangle\langle x_2x_6 \rangle\langle x_4x_5 \rangle + \langle x_1x_4 \rangle\langle x_2x_3 \rangle\langle x_5x_6 \rangle + \langle x_1x_4 \rangle\langle x_2x_5 \rangle\langle x_3x_6 \rangle + \langle x_1x_4 \rangle\langle x_2x_6 \rangle\langle x_3x_5 \rangle$$
$$+ \langle x_1x_5 \rangle\langle x_2x_3 \rangle\langle x_4x_6 \rangle + \langle x_1x_5 \rangle\langle x_2x_4 \rangle\langle x_3x_6 \rangle + \langle x_1x_5 \rangle\langle x_2x_6 \rangle\langle x_3x_4 \rangle + \langle x_1x_6 \rangle\langle x_2x_3 \rangle\langle x_4x_5 \rangle + \langle x_1x_6 \rangle\langle x_2x_4 \rangle\langle x_3x_5 \rangle$$
$$+ \langle x_1x_6 \rangle\langle x_2x_5 \rangle\langle x_3x_4 \rangle$$
$$+ \langle x_1x_2x_3 \rangle\langle x_4x_5x_6 \rangle + \langle x_1x_2x_4 \rangle\langle x_3x_5x_6 \rangle + \langle x_1x_2x_5 \rangle\langle x_3x_5x_6 \rangle + \langle x_1x_2x_6 \rangle\langle x_3x_4x_5 \rangle + \langle x_1x_3x_4 \rangle\langle x_2x_5x_6 \rangle$$
$$+ \langle x_1x_3x_5 \rangle\langle x_2x_4x_6 \rangle + \langle x_1x_3x_6 \rangle\langle x_2x_4x_5 \rangle + \langle x_1x_4x_5 \rangle\langle x_2x_3x_6 \rangle + \langle x_1x_4x_6 \rangle\langle x_2x_3x_5 \rangle + \langle x_1x_5x_6 \rangle\langle x_2x_3x_4 \rangle \quad \text{(D6)}$$

Considering $\langle \tilde{a}_{\ell_1m_1}^{\text{(CMB)}} a_{\ell_2m_2}^{\text{(CIB)}} a_{\ell_3m_3}^{\text{(CIB)}} \rangle = 0$, the correlation term (Eq. D5) is:

$$\langle b_{\ell_1\ell_2\ell_3}^{\text{CIB-Lens}} b_{\ell_1'\ell_2'\ell_3'}^{\text{CIB-Lens}} \rangle = \frac{\tilde{C}_{\ell_1}^{\text{(CMB)}} \tilde{C}_{\ell_2}^{\text{(CMB)}} C_{\ell_3}^{\text{(CIB)}}}{I_{\ell_1\ell_2\ell_3} I_{\ell_1'\ell_2'\ell_3'}} \left(\delta_{\ell_1\ell_1'} \delta_{\ell_2\ell_2'} \delta_{\ell_3\ell_3'} + \delta_{\ell_1\ell_2'} \delta_{\ell_1'\ell_2} \delta_{\ell_3\ell_3'}\right) +$$
$$+ \frac{\langle b_{\ell_1\ell_2\ell_3}^{\text{CIB-Lens}} \rangle \langle b_{\ell_1'\ell_2'\ell_3'}^{\text{CIB-Lens}} \rangle}{I_{\ell_1\ell_2\ell_3} I_{\ell_1'\ell_2'\ell_3'}} \left(1 + \frac{\delta_{\ell_3\ell_3'}}{2\ell_3+1} + \frac{\delta_{\ell_1'\ell_2}}{2\ell_2+1} + \frac{\delta_{\ell_2\ell_2'}}{2\ell_2+1} + \frac{\delta_{\ell_1\ell_2'}}{2\ell_1+1} + \frac{\delta_{\ell_1\ell_1'}}{2\ell_1+1}\right), \quad \text{(D7)}$$

and therefore, the covariance of the bispectrum is:

$$\text{cov}\left(b_{\ell_1\ell_2\ell_3}^{\text{(CIB-Lens)}}, b_{\ell_1'\ell_2'\ell_3'}^{\text{(CIB-Lens)}}\right) = \frac{\tilde{C}_{\ell_1}^{\text{(CMB)}} \tilde{C}_{\ell_2}^{\text{(CMB)}} C_{\ell_3}^{\text{(CIB)}}}{I_{\ell_1\ell_2\ell_3} I_{\ell_1'\ell_2'\ell_3'}} \left(\delta_{\ell_1\ell_1'} \delta_{\ell_2\ell_2'} \delta_{\ell_3\ell_3'} + \delta_{\ell_1\ell_2'} \delta_{\ell_1'\ell_2} \delta_{\ell_3\ell_3'}\right) +$$
$$+ \frac{\langle b_{\ell_1\ell_2\ell_3}^{\text{CIB-Lens}} \rangle \langle b_{\ell_1'\ell_2'\ell_3'}^{\text{CIB-Lens}} \rangle}{I_{\ell_1\ell_2\ell_3} I_{\ell_1'\ell_2'\ell_3'}} \left(\frac{\delta_{\ell_3\ell_3'}}{2\ell_3+1} + \frac{\delta_{\ell_1'\ell_2}}{2\ell_2+1} + \frac{\delta_{\ell_2\ell_2'}}{2\ell_2+1} + \frac{\delta_{\ell_1\ell_2'}}{2\ell_1+1} + \frac{\delta_{\ell_1\ell_1'}}{2\ell_1+1}\right), \quad \text{(D8)}$$

We consider the diagonal and non diagonal terms

$$\text{cov}\left(b_{\ell_1\ell_2\ell_3}^{\text{(CIB-Lens)}}, b_{\ell_1\ell_2\ell_3}^{\text{(CIB-Lens)}}\right) = \frac{2\tilde{C}_{\ell_1}^{\text{(CMB)}} \tilde{C}_{\ell_2}^{\text{(CMB)}} C_{\ell_3}^{\text{(CIB)}}}{I_{\ell_1\ell_2\ell_3}^2} + \frac{\langle b_{\ell_1\ell_2\ell_3}^{\text{CIB-Lens}} \rangle \langle b_{\ell_1\ell_2\ell_3}^{\text{CIB-Lens}} \rangle}{I_{\ell_1\ell_2\ell_3}^2} \left(\frac{2}{2\ell_1+1} + \frac{2}{2\ell_2+1} + \frac{1}{2\ell_3+1}\right),$$
$$\text{cov}\left(b_{\ell_1\ell_2\ell_3}^{\text{(CIB-Lens)}}, b_{\ell_1'\ell_2'\ell_3'}^{\text{(CIB-Lens)}}\right) = \frac{\langle B_{\ell_1\ell_2\ell_3}^{\text{CIB-Lens}} \rangle \langle B_{\ell_1'\ell_2'\ell_3'}^{\text{CIB-Lens}} \rangle}{I_{\ell_1\ell_2\ell_3} I_{\ell_1'\ell_2'\ell_3'}} \left(\frac{\delta_{\ell_3\ell_3'}}{2\ell_3+1} + \frac{\delta_{\ell_1'\ell_2}}{2\ell_2+1} + \frac{\delta_{\ell_2\ell_2'}}{2\ell_2+1} + \frac{\delta_{\ell_1\ell_2'}}{2\ell_1+1} + \frac{\delta_{\ell_1\ell_1'}}{2\ell_1+1}\right). \quad \text{(D9)}$$

We have estimated that

$$\frac{\langle b_{\ell_1\ell_2\ell_3}^{\text{(CIB-Lens)}} \rangle^2 I_{\ell_1\ell_2\ell_3}^2}{\tilde{C}_{\ell_1}^{\text{(CMB)}} \tilde{C}_{\ell_2}^{\text{(CMB)}} C_{\ell_3}^{\text{(CIB)}}} \leqslant 10^{-5}, \quad \text{(D10)}$$

depending on the frequency (see Table D1). Furthermore

$$\frac{\langle b_{\ell_1\ell_2\ell_3}^{\text{(CIB-Lens)}} \rangle \langle b_{\ell_1'\ell_2'\ell_3'}^{\text{(CIB-Lens)}} \rangle I_{\ell_1\ell_2\ell_3} I_{\ell_1'\ell_2'\ell_3'}}{\sqrt{\tilde{C}_{\ell_1}^{\text{(CMB)}} \tilde{C}_{\ell_2}^{\text{(CMB)}} C_{\ell_3}^{\text{(CIB)}} \tilde{C}_{\ell_1'}^{\text{(CMB)}} \tilde{C}_{\ell_2'}^{\text{(CMB)}} C_{\ell_3'}^{\text{(CIB)}}}} \leqslant 10^{-5}, \quad \text{(D11)}$$

Table D1. Maximum value for the ratio of the CIB–lensing bispectrum and its dispersion, $\max\left(\frac{\langle B^{(\text{CIB}-\text{Lens})}_{\ell_1\ell_2\ell_3}\rangle^2}{(1+\delta_{\ell_1\ell_2})\tilde{C}^{(\text{CMB})}_{\ell_1}\tilde{C}^{(\text{CMB})}_{\ell_2}C^{(\text{CIB})}_{\ell_3}}\right)$, for the *Planck* raw maps at different frequencies including instrumental beams and noise.

Frequency (GHz)	$\nu_{\text{CMB}} = 100$	$\nu_{\text{CMB}} = 143$	$\nu_{\text{CMB}} = 217$	$\nu_{\text{CMB}} = 353$	$\nu_{\text{CMB}} = 545$	$\nu_{\text{CMB}} = 857$
$\nu_{\text{CIB}} = 143$	4.49×10^{-6}	4.50×10^{-6}	4.49×10^{-6}	4.46×10^{-6}	2.49×10^{-6}	2.61×10^{-8}
$\nu_{\text{CIB}} = 217$	8.84×10^{-6}	$9.74. \times 10^{-6}$	9.47×10^{-6}	8.77×10^{-6}	4.46×10^{-6}	4.38×10^{-8}
$\nu_{\text{CIB}} = 353$	1.45×10^{-5}	2.25×10^{-5}	2.19×10^{-5}	1.26×10^{-5}	5.92×10^{-6}	5.20×10^{-8}
$\nu_{\text{CIB}} = 545$	1.29×10^{-5}	1.83×10^{-5}	1.78×10^{-5}	1.18×10^{-5}	5.94×10^{-6}	5.64×10^{-8}
$\nu_{\text{CIB}} = 857$	1.36×10^{-5}	2.14×10^{-5}	2.08×10^{-5}	1.17×10^{-5}	4.76×10^{-6}	5.47×10^{-8}

and the same replacing in Eq. (D11) any of the pairs of bispectra given in Eq. (D9). This means that the off diagonal elements of the covariance matrix are small, compared to the diagonal. If we normalise it by the diagonal, it is then of the form $\widehat{\text{cov}} = \mathbb{1} + \varepsilon$ where $\mathbb{1}$ is the unit matrix and the hat denotes the normalisation, $\widehat{\text{cov}}_{ij} = \text{cov}_{ij}/\sqrt{\text{cov}_{ii}\text{cov}_{jj}}$. The inverse can be approximated by a series expansion,

$$\widehat{\text{cov}}^{-1} = (\mathbb{1} + \varepsilon)^{-1} = \mathbb{1} - \varepsilon + \mathcal{O}\left(\varepsilon^2\right), \tag{D12}$$

i.e. the off diagonal elements of the inverse of the normalised covariance matrix are also small, of the same order as the off diagonal elements of the normalised covariance matrix. To understand whether the off diagonal elements can become relevant we can thus look at $\mathbb{1} - \varepsilon$, or since the signs of the off diagonal elements are fairly random, directly at the covariance matrix, without the need to perform an explicit inversion of an impossibly large matrix. Now, *if* the signs of the off diagonal elements are random, then their sum grows only like the square-root of the number of elements. So even though there are many more off diagonal terms than diagonal terms, their total contribution should still remain sub-dominant. To test whether this is the case, we have summed up the off diagonal terms of the normalised matrix along rows, for $\ell_{\max} = 2000$. We find that the sum is always smaller than 0.1. The mean value of the sums is of the order of 10^{-5}, with a standard deviation of 1.2×10^{-3}, which supports the assumption that the signs are relatively random, and shows that the majority of the row sums are small (indeed, 95% are smaller, in absolute terms, than 1.5×10^{-3} as the distribution of row-sum values is quite non-Gaussian). Therefore, the covariance can be approximated by the Gaussian part:

$$\text{cov}\left(b^{(\text{CIB}-\text{Lens})}_{\ell_1\ell_2\ell_3}, b^{(\text{CIB}-\text{Lens})}_{\ell'_1\ell'_2\ell'_3}\right) \simeq \frac{\tilde{C}^{(\text{CMB})}_{\ell_1}\tilde{C}^{(\text{CMB})}_{\ell_2}C^{(\text{CIB})}_{\ell_3}}{I_{\ell_1\ell_2\ell_3}I_{\ell'_1\ell'_2\ell'_3}}\left(\delta_{\ell_1\ell'_1}\delta_{\ell_2\ell'_2}\delta_{\ell_3\ell'_3} + \delta_{\ell_1\ell'_2}\delta_{\ell_1\ell'_2}\delta_{\ell_3\ell'_3}\right).$$